Geochemistry Geophysics Geosystems G3
AN ELECTRONIC JOURNAL OF THE EARTH SCIENCES
Published by AGU and the Geochemical Society

Article
Volume 7, Number 12
19 December 2006
Q12007, doi:10.1029/2006GC001290
ISSN: 1525-2027

Submarine Fernandina: Magmatism at the leading edge of the Galápagos hot spot

Dennis J. Geist
Department of Geological Sciences, University of Idaho 3022, Moscow, Idaho 83844, USA (dgeist@uidaho.edu)

Daniel J. Fornari
Geology and Geophysics Department, Woods Hole Oceanographic Institution, Woods Hole, Massachusetts 02543, USA

Mark D. Kurz
Marine Chemistry and Geochemistry Department, Woods Hole Oceanographic Institution, Woods Hole, Massachusetts 02543, USA

Karen S. Harpp
Geology Department, Colgate University, Hamilton, New York 13348, USA

S. Adam Soule
Geology and Geophysics Department, Woods Hole Oceanographic Institution, Woods Hole, Massachusetts 02543, USA

Michael R. Perfit
Department of Geological Sciences, University of Florida, Gainesville, Florida 32611, USA

Alison M. Koleszar
Department of Geosciences, Brown University, Providence, Rhode Island 02912, USA

[1] New multibeam and side-scan sonar surveys of Fernandina volcano and the geochemistry of lavas provide clues to the structural and magmatic development of Galápagos volcanoes. Submarine Fernandina has three well-developed rift zones, whereas the subaerial edifice has circumferential fissures associated with a large summit caldera and diffuse radial fissures on the lower slopes. Rift zone development is controlled by changes in deviatoric stresses with increasing distance from the caldera. Large lava flows are present on the gently sloping and deep seafloor west of Fernandina. Fernandina's submarine lavas are petrographically more diverse than the subaerial suite and include picrites. Most submarine glasses are similar in composition to aphyric subaerially erupted lavas, however. These rocks are termed the "normal" series and are believed to result from cooling and crystallization in the subcaldera magma system, which buffers the magmas both thermally and chemically. These normal-series magmas are extruded laterally through the flanks of the volcano, where they scavenge and disaggregate olivine-gabbro mush to produce picritic lavas. A suite of lavas recovered from the terminus of the SW submarine rift and terraces to the south comprises evolved basalts and icelandites with MgO = 3.1 to 5.0 wt.%. This "evolved series" is believed to form by fractional crystallization at 3 to 5 kb, involving extensive crystallization of clinopyroxene and titanomagnetite in addition to plagioclase. "High-K" lavas were recovered from the southwest rift and are attributed to hybridization between normal-series basalt and evolved-series magma. The geochemical and structural findings are used to develop an evolutionary model for the construction of

the Galápagos Platform and better understand the petrogenesis of the erupted lavas. The earliest stage is represented by the deep-water lava flows, which over time construct a broad submarine platform. The deep-water lavas originate from the subcaldera plumbing system of the adjacent volcano. After construction of the platform, eruptions focus to a point source, building an island with rift zones extending away from the adjacent, buttressing volcanoes. Most rift zone magmas intrude laterally from the subcaldera magma chamber, although a few evolve by crystallization in the upper mantle and deep crust.

Components: 14,969 words, 15 figures, 4 tables.

Keywords: rift zone; magmatic; evolution; Galápagos.

Index Terms: 3615 Mineralogy and Petrology: Intra-plate processes (1033, 8415); 8415 Volcanology: Intra-plate processes (1033, 3615); 8427 Volcanology: Subaqueous volcanism.

Received 26 February 2006; **Revised** 15 September 2006; **Accepted** 20 September 2006; **Published** 19 December 2006.

Geist, D. J., D. J. Fornari, M. D. Kurz, K. S. Harpp, S. A. Soule, M. R. Perfit, and A. M. Koleszar (2006), Submarine Fernandina: Magmatism at the leading edge of the Galápagos hot spot, *Geochem. Geophys. Geosyst.*, *7*, Q12007, doi:10.1029/2006GC001290.

1. Introduction

[2] Geodynamic theories of the Earth's mantle, including its early history, the scale of convection, and its composition, have been strongly influenced by the study of seamounts and the submarine flanks of ocean island volcanoes [e.g., *Allegre et al.*, 1983; *White*, 1985; *Hofmann*, 1997]. For example, lavas from Loihi seamount, at the leading edge of the Hawaiian hot spot, have provided unique insight into the petrogenesis of mantle-derived magma. Loihi also provides a window into the nascent evolutionary stages of an ocean-island volcano [e.g., *Moore et al.*, 1982; *Malahoff*, 1987, *Fornari et al.*, 1988; *Garcia et al.*, 1998]. Studies of submarine Hawaiian rift zones have also increased our understanding of the structure, morphology, and magmatic plumbing systems of Hawaiian volcanoes by providing samples of lavas that are older than those exposed on land, and younger lavas that have bypassed the shallow storage reservoir [e.g., *Fornari et al.*, 1979; *Fornari and Campbell*, 1987; *Lonsdale*, 1989; *Garcia et al.*, 1995; *Clague et al.*, 1995; *Lipman et al.*, 1988, 2002; *Smith et al.*, 2002; *Sisson et al.*, 2002].

[3] The primary objective of this study is to characterize the style of submarine volcanism in the western Galápagos and identify the tectonic and magmatic processes responsible for the earliest phases of volcanism as the Nazca plate passes over the Galápagos hot spot (Figure 1). Fernandina volcano is the most active in the Galápagos Archipelago, with 23 witnessed eruptions in the past 2 centuries [*Simkin and Siebert*, 1994], the most recent in May 2005. This prolific volcanic activity, the eastward motion of the Nazca plate [*Gripp and Gordon*, 2002], and the high $^3He/^4He$ ratios of Fernandina lavas [*Graham et al.*, 1993; *Kurz and Geist*, 1999] suggest that Fernandina volcano overlies the Galápagos hot spot. Recent seismic studies, including tomographic inversions of body waves [*Toomey et al.*, 2001], surface wave tomography (D. Villagomez et al., Upper mantle structure beneath the Galápagos from surface wave tomography, submitted to *Journal of Geophysical Research*, 2006), and documentation of transition zone thinning [*Hooft et al.*, 2003], have confirmed that the Galápagos plume traverses the upper mantle southwest of Fernandina's surface position.

[4] The subaerial flanks of the western Galápagos shields, as typified by Fernandina, differ from Hawaiian shields in numerous respects. Fernandina lacks the focused subaerial rift zones that characterize Hawaiian shields [e.g., *Fiske and Jackson*, 1972]. Instead, in the summit region, eruptive vents lie along fissures that are subparallel to the caldera walls, whereas on the lower flanks fissures are radial [*Simkin*, 1972; *Chadwick and Howard*, 1991; *Rowland*, 1996]. Although radial fissures are concentrated in some sectors of the subaerial edifice (e.g., Fernandina's northwest sector), these zones of fissuring are diffuse and distributed over an area several kilometers wide across strike [*Chadwick and Howard*, 1991]. Fernandina's caldera dominates the volcano's summit and is 850 m deep and $\sim$32 km^2 in area. The caldera remains in active formation, having dropped $\sim$300 m in 1968 [*Simkin and Howard*, 1970]. Galápagos calderas

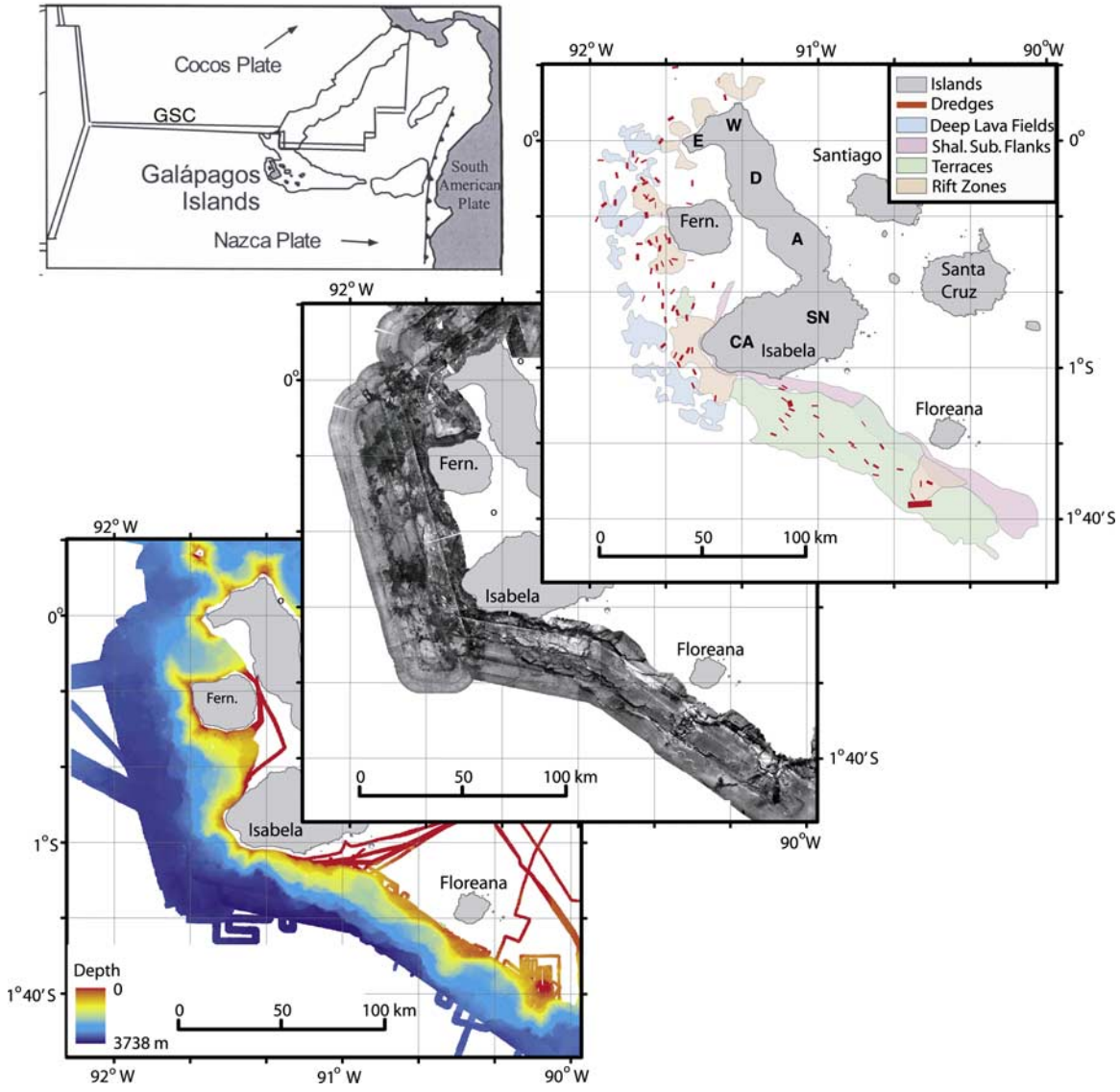

Figure 1. Triptych of maps showing (bottom) multibeam bathymetry compilation, (middle) MR1 side-scan sonar, and (top) general geological interpretation of the study area along the western margin of the Galápagos platform. MR1 side-scan imagery is processed to show strong reflectors as dark gray to black and low reflectivity or acoustic shadow as gray or white. Top left inset shows the tectonic setting and location of the Galápagos archipelago; arrows indicate plate motion. Dredge locations are indicated on the geologic map in red. CA, Cerro Azul; SN, Sierra Negra; A, Alcedo; D, Darwin; W, Wolf; E, Ecuador.

are thought to be underlain by shallow sills (<3 km deep), which contain most of the subaerially erupted magma before eruption [*Amelung et al.*, 2000; *Geist et al.*, 2006]. Fernandina's subaerial lavas consist of homogeneous, evolved tholeiitic basalt [*Allan and Simkin*, 2000], rich in plagioclase and poor in olivine.

[5] The submarine geology and bathymetry around the Galápagos Islands were poorly known and sparsely sampled prior to this study. Prior work was limited to widely spaced multibeam mapping and dredging of the platform and the region between the central Galápagos and the Galápagos Spreading Center (GSC) during the PLUME02 cruise in 1990 [*Christie et al.*, 1992]. This paper presents new details on the submarine geology of Fernandina volcano, including volcanic features not previously described at other hot spot provinces and the petrology of its submarine lavas. These findings are used to formulate a new model for the

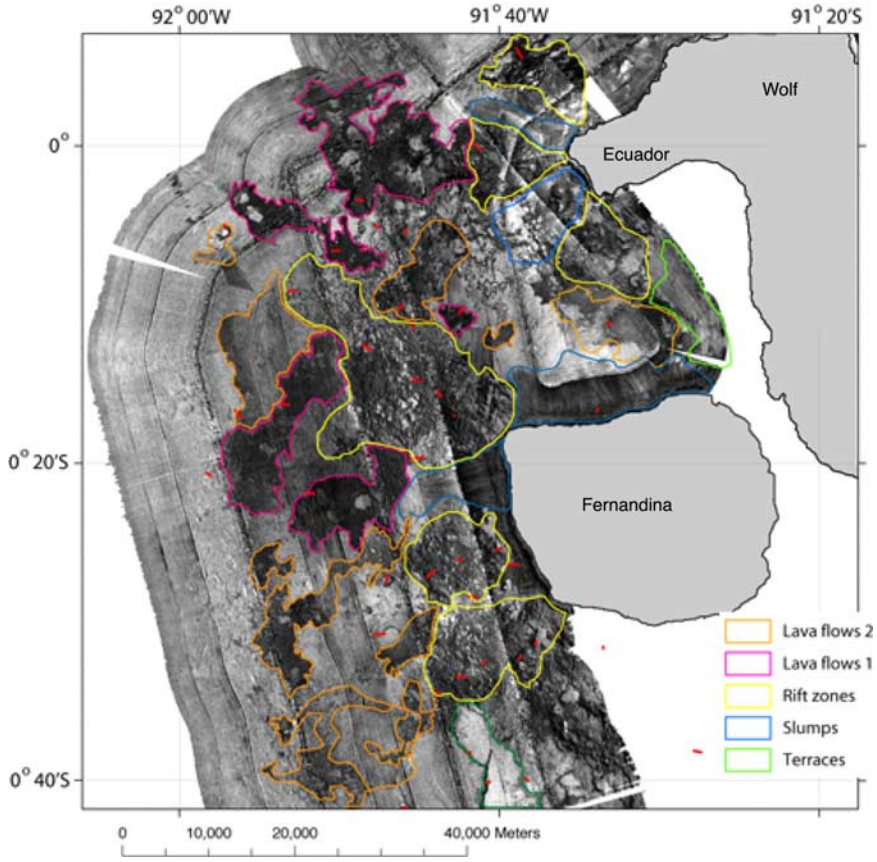

Figure 2. Detail of side-scan sonar imagery around Fernandina volcano. Strong reflectors are shown as dark gray to black, and low reflectivity or acoustic shadow are shown as gray or white. Geologic interpretations are overlain. Dredge locations are indicated in red. Large lava flows are divided into an older unit (Lava flows 2) and younger unit (Lava flows 1).

growth and petrologic evolution of Galápagos volcanoes.

2. Methods

[6] Multibeam bathymetric and side-scan sonar data of Fernandina's flanks were acquired on two cruises in 2000 and 2001 using the R/V *Melville* (AHA-Nemo2 cruise) and R/V *Revelle* (DRIFT4 cruise), and considerable effort was made to merge previous multibeam data [*Christie et al.*, 1992] into our compiled grids. We use AHA-Nemo2 data as the controlling grid because of its superior signal-to-noise ratio, general lack of artifacts, and excellent coverage around Fernandina. DRIFT4 multibeam data were affected by noise, which degraded the resulting grids. Modest filtering was applied but visible artifacts remain in parts of the bathymetric maps, especially in deep-water flat terrain where signal-to-noise was low (Figure 2). Side-scan sonar data were acquired with the University of Hawaii MR1 11/12 kHz towed sonar system [e.g., *Rongstadt*, 1992] (http://www.soest.hawaii.edu/HMRG/MR1/index.html) on the 2001 DRIFT4 cruise simultaneously with multibeam acquisition. Side-scan swaths are ~10 km wide, and data were gridded at 8 m pixel resolution (Figure 2). Ship navigation was by P-Code GPS with correction applied to the side-scan data for layback of the towfish behind the ship. Resulting side-scan mosaics are considered to have overall geodetic accuracy of ~20–50 m, which increases with decreasing distance to the sonar nadir.

[7] Rocks were collected on both the AHA-Nemo-2 (14 dredges at Fernandina; "AHA" prefix in Tables 1–4) and DRIFT4 cruises by dredging (20 dredges at Fernandina; samples with a "D" prefix in Tables 1–4) and using a wax-corer (5 sites; "RC" prefix) (Figure 3). Several of the dredges retrieved no sizable rocks, but small fragments were collected in a weighted burlap bag that was tied into

Table 1. Sample Locations

		Latitude S		Longitude W			Latitude S		Longitude W	
Dredge	Start Depth, m	deg	min	deg	min	End Depth, m	deg	min	deg	min
AHA 18	2550	0	10.00	91	46.00	2450	0	10.36	91	46.37
AHA 19	2930	0	12.50	91	48.60	2670	0	12.92	91	47.97
AHA 20	1840	0	14.73	91	45.33	1640	0	14.58	91	45.19
AHA 21	1700	0	14.73	91	45.09	1640	0	14.88	91	44.88
AHA 22	2390	0	10.97	91	45.67	2210	0	11.54	91	45.38
AHA 23	1490	0	15.36	91	43.91	1300	0	15.85	91	43.64
AHA 24	3260	0	27.00	91	47.05	2970	0	27.53	91	47.07
AHA 25	2900	0	27.20	91	44.60	2600	0	26.72	91	43.94
AHA 26	2000	0	26.10	91	42.70	1780	0	26.06	91	42.25
AHA 27	1090	0	25.47	91	40.27	810	0	25.36	91	39.84
AHA 28	1000	0	31.50	91	37.74	800	0	31.14	91	37.69
AHA 29	1450	0	32.37	91	38.87	1200	0	32.15	91	38.59
AHA 30	1925	0	32.63	91	41.12	1780	0	32.41	91	40.84
AHA 31	900	0	31.73	91	33.50	700	0	31.50	91	33.51
AHA 32	2610	0	33.48	91	42.46	2380	0	33.44	91	42.14
D7	3025	0	3.41	91	49.00	2949	0	3.45	91	48.46
D8	2723	0	5.22	91	45.98	2585	0	5.60	91	45.80
D9	3115	0	6.60	91	50.50	3058	0	6.60	91	49.94
D10	3227	0	4.92	91	57.20	2973	0	5.30	91	57.20
D11	2858	0	5.00	91	47.90	2825	0	5.18	91	47.52
D12	1144	0	16.52	91	33.89	934	0	16.80	91	33.90
D13	2147	0	11.20	91	33.37	1958	0	11.20	91	32.89
D14	2463	0	10.16	91	42.13	2445	0	10.60	91	42.58
D15	1243	0	17.01	91	42.93	1142	0	17.01	91	42.73
D16	1430	0	19.62	91	41.36	1306	0	19.60	91	41.20
D17	3388	0	21.89	91	52.20	3353	0	21.90	91	51.50
D18	3421	0	20.61	91	58.37	3324	0	20.79	91	58.00
D19	3396	0	16.60	91	56.57	3400	0	17.20	91	56.09
D20	3385	0	16.30	91	53.78	3365	0	16.30	91	53.09
D21	3242	0	9.19	91	53.27	3214	0	9.08	91	52.69
D24	2960	0	19.75	91	45.63	2556	0	19.60	91	44.70
D25	2515	0	28.40	91	42.00	2181	0	28.49	91	41.35
D26	3321	0	30.75	91	47.90	3076	0	30.75	91	47.10
D27	3195	0	34.41	91	44.17	2960	0	34.50	91	43.70
D28	1216	0	26.40	91	39.49	851	0	26.39	91	38.75
D29	3261	0	38.20	91	42.23	3064	0	38.22	91	41.73
D30	3218	0	40.15	91	41.03	2964	0	40.10	91	40.55
D31	2963	0	39.82	91	38.46	2727	0	40.05	91	38.10
D32	2881	0	44.16	91	38.38	2435	0	44.40	91	37.84
D33	3472	0	41.66	91	46.12	3327	0	41.75	91	45.75
D34	3245	0	47.40	91	40.43	2852	0	47.30	91	39.86
D35	3235	0	43.60	91	41.24	2964	0	43.60	91	40.55
D36	2790	0	45.54	91	37.38	2499	0	45.33	91	36.70
D37	1567	0	38.10	91	27.90	1166	0	38.21	91	27.31
D38	2346	0	43.60	91	33.19	2154	0	43.80	91	32.60
D39	2281	0	46.85	91	34.84	2155	0	46.80	91	34.30
D40	3096	0	53.93	91	40.98	3097	0	54.46	91	40.58
RC-01	3215	0	4.00	91	54.30					
RC-02	3427	0	20.90	91	55.05					
RC-03	3427	0	20.90	91	55.05					
RC-04	3298	0	23.25	91	50.19					
RC-05	3239	0	21.50	91	47.90					
RC-07	1269	0	36.44	91	32.14					

Table 2. Electron Microprobe Analyses of Fernandina Glasses[a]

Sample	Mg#	SiO_2	TiO_2	Al_2O_3	FeO	MgO	CaO	Na_2O	K_2O	P_2O_5	S	MnO	Total
AHA18 A	51.1	49.15	2.97	14.09	11.68	6.85	11.53	2.73	0.44	0.38	0.10	0.06	97.83
AHA18 B	51.1	49.07	2.96	14.04	11.76	6.89	11.54	2.76	0.45	0.37	0.10	0.05	97.50
AHA18 C	51.0	49.29	2.99	13.95	11.75	6.85	11.37	2.82	0.45	0.37	0.11	0.04	97.73
AHA19 A	50.0	49.48	2.98	13.95	11.92	6.68	11.26	2.75	0.44	0.36	0.10	0.07	97.59
AHA19 B	49.6	49.60	2.98	13.90	11.92	6.59	11.24	2.75	0.45	0.36	0.12	0.07	97.26
AHA19 C	50.0	49.49	2.95	13.96	11.80	6.62	11.30	2.84	0.45	0.37	0.12	0.09	97.07
AHA19 D	49.9	49.59	3.00	13.93	11.86	6.62	11.20	2.79	0.45	0.38	0.10	0.07	97.03
AHA19 E	50.3	49.39	2.93	13.94	11.88	6.75	11.35	2.78	0.44	0.36	0.12	0.05	97.66
AHA19 F	50.7	49.54	2.94	14.02	11.67	6.74	11.37	2.80	0.43	0.37	0.05	0.05	97.20
AHA20 A	50.0	49.02	3.33	14.02	11.70	6.56	11.22	2.97	0.48	0.44	0.04	0.22	97.06
AHA20 B	48.5	48.89	3.50	13.86	11.99	6.34	11.08	3.09	0.53	0.47	0.04	0.21	97.31
AHA20 C	49.6	48.92	3.48	13.92	11.74	6.47	11.24	3.02	0.50	0.46	0.06	0.20	97.34
AHA20 D	49.4	49.12	3.45	13.88	11.76	6.44	11.15	2.97	0.51	0.44	0.06	0.21	97.22
AHA20 E	48.6	48.90	3.60	13.82	11.97	6.35	11.11	3.00	0.52	0.48	0.05	0.19	97.29
AHA20 F	49.8	48.97	3.50	13.92	11.69	6.50	11.19	3.02	0.52	0.45	0.04	0.19	97.08
AHA20 I	49.6	49.30	3.44	13.97	11.69	6.46	11.13	2.96	0.51	0.47	0.01	0.06	97.64
AHA21 A	49.3	49.13	3.48	13.85	11.81	6.44	11.14	2.95	0.52	0.46	0.05	0.16	98.03
AHA21 B	49.7	49.18	3.50	13.90	11.69	6.47	11.16	3.03	0.52	0.47	0.04	0.04	97.78
AHA21 C	48.9	49.05	3.54	13.85	11.89	6.37	11.08	3.12	0.53	0.46	0.04	0.07	98.35
AHA22 A	52.9	48.69	2.99	14.76	11.15	7.02	11.51	2.87	0.45	0.39	0.01	0.16	97.05
AHA22 B	52.8	48.79	3.01	14.65	11.24	7.06	11.44	2.86	0.45	0.39	0.02	0.09	97.20
AHA22 C	52.8	48.77	3.00	14.71	11.26	7.07	11.37	2.87	0.46	0.38	0.03	0.07	96.93
AHA22 D	53.1	48.82	2.99	14.77	11.10	7.05	11.47	2.88	0.45	0.40	0.01	0.05	97.01
AHA22 E	52.5	48.71	3.03	14.67	11.35	7.02	11.44	2.86	0.45	0.38	0.03	0.05	97.34
AHA23 A	50.9	49.37	3.16	13.91	11.59	6.73	11.39	2.81	0.42	0.39	0.02	0.22	98.03
AHA23 B	51.0	49.36	3.18	14.01	11.52	6.72	11.45	2.71	0.42	0.39	0.04	0.21	97.67
AHA23 C	48.4	49.13	3.25	14.07	11.88	6.25	11.23	3.07	0.46	0.42	0.02	0.20	97.87
AHA23 D	48.0	49.09	3.28	14.01	12.01	6.23	11.26	2.97	0.46	0.44	0.03	0.21	97.79
AHA25 A	49.9	48.94	3.32	14.06	11.81	6.61	11.32	2.80	0.47	0.37	0.13	0.15	97.99
AHA25 B	52.6	49.11	3.24	13.84	11.41	7.10	11.64	2.65	0.46	0.34	0.06	0.15	98.43
AHA25 C	48.9	48.82	3.42	14.05	12.03	6.44	11.23	2.93	0.49	0.37	0.10	0.12	97.61
AHA25 D	49.5	49.02	3.37	13.98	11.78	6.47	11.30	2.90	0.48	0.35	0.14	0.22	97.33
AHA26 A	51.0	48.82	3.21	14.01	11.67	6.82	11.48	2.87	0.44	0.35	0.11	0.22	98.38
AHA26 B	49.7	48.88	3.40	13.89	11.87	6.58	11.34	2.90	0.47	0.38	0.11	0.19	97.86
AHA26 C	51.2	48.93	3.23	14.15	11.62	6.83	11.44	2.70	0.45	0.36	0.12	0.18	98.32
AHA26 D	50.8	48.78	3.24	14.12	11.73	6.78	11.49	2.75	0.45	0.36	0.12	0.16	98.63
AHA27 A	46.7	49.69	3.54	13.72	12.30	6.04	10.76	2.83	0.52	0.40	0.07	0.12	97.99
AHA27 B	46.6	49.25	3.66	13.79	12.35	6.05	10.68	2.99	0.55	0.40	0.08	0.21	97.17
AHA27 C	46.7	49.44	3.67	13.73	12.25	6.01	10.68	2.99	0.54	0.40	0.11	0.20	97.53
AHA27 D	46.5	49.29	3.68	13.65	12.45	6.07	10.67	2.97	0.54	0.40	0.11	0.17	97.68
AHA27 E	45.2	49.21	3.70	13.56	12.70	5.88	10.58	3.14	0.56	0.41	0.12	0.14	98.23
AHA27 F	46.5	49.27	3.63	13.69	12.40	6.05	10.68	3.06	0.55	0.41	0.09	0.16	97.79
AHA28 A	37.9	50.63	3.21	16.08	10.84	3.71	7.00	5.10	2.20	1.06	0.04	0.12	96.27
AHA28 B	37.2	50.30	3.19	15.97	11.22	3.73	6.95	5.19	2.15	1.08	0.05	0.18	96.88
AHA28 C	36.8	50.32	3.22	16.12	11.16	3.65	7.00	5.08	2.15	1.06	0.05	0.19	96.73
AHA28 D	36.8	50.32	3.22	16.12	11.16	3.65	7.00	5.08	2.15	1.06	0.04	0.19	96.19
AHA29 A	45.0	49.28	3.80	13.94	12.38	5.69	10.67	3.12	0.52	0.40	0.03	0.19	96.48
AHA29 B	44.5	49.42	3.85	13.67	12.47	5.62	10.60	3.17	0.51	0.41	0.05	0.24	96.85
AHA29 C	45.0	48.85	3.78	13.78	12.75	5.85	10.61	3.24	0.50	0.41	0.04	0.18	96.18
AHA29 D	46.2	49.09	3.83	13.52	12.52	6.04	10.65	3.18	0.51	0.44	0.03	0.20	96.27
AHA29 E	45.4	49.18	3.82	13.54	12.62	5.88	10.77	3.09	0.52	0.42	0.03	0.12	96.20
AHA30 A	52.5	49.92	2.97	13.99	11.09	6.86	11.60	2.72	0.38	0.31	0.01	0.15	97.82
AHA30 B	52.0	49.51	2.91	14.17	11.34	6.90	11.49	2.77	0.39	0.32	0.04	0.15	97.21
AHA30 C	52.2	49.78	2.95	14.10	11.16	6.83	11.56	2.70	0.40	0.28	0.03	0.22	97.21
AHA30 D	51.6	49.52	3.10	14.25	11.09	6.64	11.58	2.84	0.44	0.33	0.05	0.15	97.20
AHA31A	41.5	47.67	4.16	15.53	12.89	4.51	8.22	3.95	1.77	0.86	0.09	0.25	98.98
AHA32 A		49.20	3.01	14.71	10.88	7.05	11.42	2.78	0.42	0.30	0.01	0.21	96.60
AHA32 B	54.2	49.38	2.91	14.75	10.66	7.07	11.44	2.82	0.42	0.32	0.04	0.20	96.54
AHA32 C	54.4	49.27	2.90	14.85	10.72	7.16	11.51	2.69	0.40	0.33	0.01	0.17	97.51
AHA32 D	53.9	49.12	2.92	14.93	10.85	7.12	11.37	2.78	0.42	0.32	0.02	0.15	97.31
AHA32 E	53.6	49.48	3.05	14.32	10.87	7.05	11.52	2.77	0.42	0.32	0.01	0.17	97.29
AHA32 F	53.8	49.09	2.94	14.84	10.87	7.11	11.47	2.81	0.41	0.32	0.03	0.12	97.06

Table 2. (continued)

Sample	Mg#	SiO_2	TiO_2	Al_2O_3	FeO	MgO	CaO	Na_2O	K_2O	P_2O_5	S	MnO	Total
D9 A	50.9	49.16	3.08	14.69	11.20	6.50	11.50	2.54	0.47	0.53	0.14	0.19	98.99
D11 A	51.4	48.43	3.12	14.43	11.23	6.65	12.17	2.85	0.46	0.29	0.16	0.20	98.31
D12 bur 1	45.1	48.56	3.75	13.37	12.96	5.96	11.37	2.93	0.56	0.42	0.01	0.11	98.20
D12 bur 2	44.9	48.68	3.72	13.27	13.01	5.95	11.27	2.91	0.55	0.43	0.01	0.18	97.95
D12 bur 3	44.2	48.91	3.57	13.15	13.41	5.96	10.97	3.01	0.53	0.34	0.03	0.12	98.40
D12 bur 4	45.2	48.65	3.63	13.39	13.03	6.03	11.18	2.96	0.55	0.39	0.03	0.15	99.29
D12 bur 5	44.0	49.19	3.56	12.77	13.38	5.89	11.21	2.96	0.53	0.38	0.01	0.13	97.95
D12bur 1	43.9	48.19	3.87	13.03	13.55	5.96	11.36	2.95	0.57	0.37	0.02	0.11	96.90
D12bur 2	45.0	48.36	3.78	13.12	13.24	6.08	11.47	2.93	0.55	0.35	0.02	0.11	97.57
D12bur 4	45.8	48.68	3.71	13.02	12.93	6.14	11.44	2.98	0.55	0.37	0.02	0.15	98.76
D14 A	44.1	48.40	3.86	14.56	12.16	5.37	10.73	3.43	0.69	0.41	0.18	0.23	97.90
D15 A	44.6	48.66	3.82	13.82	12.71	5.75	10.99	3.07	0.55	0.31	0.16	0.16	98.37
D15 B	41.4	48.07	4.27	12.91	13.92	5.53	10.89	3.14	0.63	0.40	0.06	0.18	98.65
D15 C	45.7	48.79	3.73	13.91	12.43	5.87	10.97	3.04	0.53	0.35	0.16	0.22	98.52
D15 D	45.1	48.54	3.79	13.82	12.64	5.81	11.04	3.09	0.56	0.36	0.15	0.20	98.13
D15 E	44.1	48.71	3.89	13.71	12.84	5.67	10.88	3.07	0.57	0.33	0.17	0.17	98.28
D16 A	39.3	48.22	4.50	12.53	14.48	5.26	10.28	3.32	0.75	0.49	0.04	0.13	99.26
D16 C	39.1	48.43	4.47	12.61	14.26	5.13	10.50	3.22	0.73	0.48	0.04	0.15	97.85
D16 E	39.1	48.48	4.43	12.58	14.28	5.14	10.39	3.26	0.72	0.47	0.04	0.20	98.14
D17 bur 1	48.9	48.49	3.47	13.51	12.33	6.61	11.75	2.71	0.48	0.33	0.12	0.19	97.86
D17 bur 2	50.0	48.38	2.98	13.56	12.29	6.90	12.28	2.70	0.45	0.26	0.01	0.19	98.13
D17 bur 3	40.1	47.87	3.59	16.59	11.93	4.48	8.29	4.36	1.69	0.87	0.11	0.21	97.15
D17 bur 4	43.4	48.51	4.11	12.69	13.60	5.85	11.07	2.97	0.59	0.37	0.03	0.20	98.70
D18 A	51.8	49.29	3.33	13.78	11.21	6.76	11.98	2.73	0.40	0.30	0.02	0.21	99.66
D19 bur 1	44.3	47.87	4.04	13.08	13.45	6.00	11.25	3.07	0.65	0.40	0.01	0.19	99.07
D19 bur 2	47.2	47.96	3.58	13.94	12.58	6.30	11.36	2.98	0.54	0.40	0.15	0.21	98.35
D20 A	39.4	48.44	4.51	12.47	14.35	5.23	10.18	3.33	0.77	0.47	0.04	0.20	99.28
D24 A	51.2	48.46	2.98	14.77	11.34	6.68	12.03	2.71	0.42	0.29	0.13	0.19	98.31
D24 B	49.6	48.67	3.05	14.68	11.56	6.38	11.82	2.80	0.41	0.28	0.13	0.21	98.02
D24 C	50.0	48.23	3.31	14.79	11.70	6.57	11.18	3.08	0.50	0.34	0.15	0.16	99.26
D24 D	51.0	48.35	2.99	14.63	11.22	6.55	11.87	3.35	0.44	0.29	0.15	0.17	98.30
D24 E	51.1	48.66	3.00	14.75	11.25	6.60	11.91	2.75	0.39	0.31	0.14	0.23	98.75
D24 F	50.0	48.36	3.19	14.57	11.75	6.60	11.51	2.94	0.47	0.30	0.13	0.19	98.82
D26 B	45.6	47.90	3.85	14.11	12.28	5.77	10.97	3.86	0.65	0.40	0.06	0.15	98.29
D26 B	46.9	48.21	3.61	13.31	12.53	6.22	11.31	3.68	0.60	0.35	0.02	0.14	98.52
D26 bur 1	46.9	48.21	3.61	13.31	12.53	6.22	11.31	3.68	0.60	0.35	0.02	0.15	99.76
D26 bur 2	53.1	48.35	3.28	14.41	11.32	7.19	11.85	2.80	0.41	0.23	0.03	0.12	99.77
D27 A	48.2	47.25	4.34	16.22	11.23	5.86	10.12	3.17	1.04	0.49	0.14	0.14	99.00
D27 C	47.7	46.95	4.36	16.14	11.40	5.84	10.23	3.24	1.05	0.46	0.15	0.18	98.35
D27 D	47.5	47.35	4.33	16.13	11.29	5.72	10.15	3.21	1.07	0.45	0.13	0.16	98.59
D27 I	47.1	47.32	4.34	15.85	11.35	5.67	10.30	3.27	1.09	0.48	0.15	0.17	98.78
D28 A	46.2	48.29	3.69	13.26	12.60	6.07	10.93	3.90	0.58	0.41	0.02	0.25	99.81
D28 C	57.4	48.01	3.17	15.57	10.03	7.59	11.92	2.72	0.42	0.23	0.08	0.25	99.40
D28 F	54.6	48.03	3.29	14.94	10.67	7.19	11.83	3.00	0.45	0.28	0.06	0.27	99.01
D28 I	49.4	47.93	3.55	13.69	11.96	6.54	11.70	3.56	0.55	0.36	0.02	0.15	98.67
D29 bur 1	45.2	48.24	3.73	12.74	13.65	6.31	11.51	2.83	0.53	0.34	0.01	0.13	99.17
D29 bur 2	41.4	48.39	4.25	12.37	14.24	5.65	10.84	3.02	0.58	0.39	0.03	0.25	99.33
D30 A	37.5	46.56	3.47	12.29	15.40	5.17	10.50	5.12	0.70	0.49	0.08	0.21	98.37
D30 B	38.6	46.80	3.32	12.49	15.12	5.34	10.59	5.00	0.68	0.46	0.08	0.12	99.03
D30 C	38.2	46.49	3.50	12.33	15.33	5.32	10.59	5.03	0.69	0.52	0.09	0.11	98.58
D30 D	38.9	46.45	3.50	12.46	15.12	5.41	10.58	5.00	0.67	0.55	0.09	0.17	98.25
D30 E	38.7	46.71	3.43	12.40	15.13	5.35	10.56	4.98	0.70	0.48	0.08	0.18	98.74
D31 A	41.4	47.84	3.70	13.13	13.75	5.46	10.32	4.44	0.65	0.43	0.16	0.10	99.37
D31 B	41.3	47.67	3.73	13.11	13.94	5.50	10.21	4.45	0.65	0.47	0.15	0.12	99.81
D31 C	41.4	47.56	3.75	13.18	13.94	5.52	10.20	4.46	0.66	0.45	0.15	0.11	99.47
D32 bur 1	38.5	50.16	3.09	16.79	11.25	3.95	7.53	4.74	1.98	0.41	0.06	0.05	99.88
D32 bur 2	45.2	48.09	3.24	13.15	13.57	6.28	11.62	3.03	0.54	0.31	0.01	0.16	98.02
D32 bur 3	42.2	47.55	4.32	12.56	14.10	5.78	10.93	3.01	0.58	0.99	0.03	0.14	98.55
D33 B	47.3	48.29	3.53	14.30	12.19	6.13	11.27	2.99	0.56	0.38	0.17	0.19	97.55
D33 C	47.4	48.29	3.54	14.41	12.08	6.10	11.28	2.97	0.55	0.40	0.17	0.21	98.38
D35 A	34.4	51.53	2.28	17.11	10.84	3.19	6.31	4.86	2.28	1.36	0.07	0.17	98.23
RC01	51.2	48.82	3.05	14.42	11.42	6.71	11.69	2.77	0.49	0.33	0.15	0.16	98.67

Table 2. (continued)

Sample	Mg#	SiO_2	TiO_2	Al_2O_3	FeO	MgO	CaO	Na_2O	K_2O	P_2O_5	S	MnO	Total
RC02	56.5	48.43	2.35	14.95	10.19	7.42	12.93	2.67	0.48	0.22	0.12	0.23	99.28
RC04	41.5	48.22	3.57	16.98	11.34	4.51	8.18	4.40	1.63	0.82	0.11	0.22	97.92
RC05	48.3	48.05	3.52	14.38	12.12	6.36	11.16	3.11	0.57	0.37	0.14	0.22	98.37
RC07	39.5	49.31	3.59	15.93	11.54	4.23	8.12	4.34	1.83	0.89	0.09	0.14	98.65
Precision RSD		0.6%	1.5%	0.7%	1.6%	1.2%	0.7%	1.9%	8.5%	9.3%	56.4%	14.5%	0.4%
AHA32A MIT		49.20	3.01	14.71	10.88	7.05	11.42	2.78	0.42	0.30	0.01	0.21	96.60
AHA32A WSU		48.52	2.93	15.26	10.69	7.00	11.82	2.75	0.44	0.30	0.11	0.18	96.27

[a] Analytical techniques are described in text. Oxides are in weight% and normalized to 100%. Reported total is as analyzed. Sulfur is reported as elemental sulfur, and all iron is reported as ferrous iron.

the bottom of each dredge's chain bag; these samples are indicated with the suffix "bur". All samples were sorted, catalogued, and rinsed in fresh water immediately after collection, and where possible, glass chips were removed for geochemical analysis.

[8] Major element analyses of glasses (Table 2) and phenocrysts were accomplished by electron microprobe. AHA glasses were analyzed at MIT on a JEOL JXA-733 Superprobe, whereas DRIFT4 glasses and phenocrysts were analyzed on the Cameca Camebax microprobe at Washington State University. For all glasses, accelerating voltage was 15 kV, beam current was 20 μa, a defocused beam was used, and sodium intensity was monitored as a function of time and corrected for volatilization, although this correction was not significant. For most glasses, two points on three separate shards were measured and averaged. A comparison of analyses determined on the same sample using MIT and WSU analytical facilities is reported in Table 2, as is estimated precision. Some mineral compositions were determined with a Cameca SX50 microprobe at the University of Hawaii using techniques described by *Garcia et al.* [1995]. Whole rock analyses were by XRF in the Washington State University Geoanalytical Laboratory (Table 3), using the technique described by *Johnson et al.* [1999]. Trace elements were determined by ICP-MS at Colgate University, using techniques described by *Harpp et al.* [2003], and precisions are reported in Table 4.

3. Geology of Submarine Fernandina

[9] The submarine flanks of Fernandina and adjacent deep-water areas comprise five acoustic provinces mapped using MR1 data. In some cases, the acoustic provinces also conform to variations in the

Table 3. Whole Rock Analyses by XRF[a]

Sample	SiO_2	TiO_2	Al_2O_3	FeO	MgO	CaO	Na_2O	K_2O	P_2O_5	MnO	Total
AHA18 A	48.22	2.19	15.76	9.44	9.24	12.00	2.37	0.39	0.23	0.16	100.23
AHA19 A	47.92	1.83	13.43	9.67	13.98	10.24	2.24	0.34	0.19	0.16	101.53
AHA20 A	48.62	2.76	16.53	9.87	6.68	11.85	2.76	0.47	0.30	0.16	99.86
AHA21 A	48.79	2.73	16.86	9.56	6.49	11.94	2.78	0.49	0.30	0.05	99.52
AHA22 A	47.95	2.49	15.38	10.23	9.54	11.03	2.56	0.47	0.27	0.07	99.67
AHA23 A	49.39	2.52	16.06	9.63	6.66	12.08	2.86	0.39	0.25	0.16	100.43
AHA25 A	47.64	1.90	16.06	8.95	11.09	11.57	2.13	0.33	0.19	0.15	99.68
AHA26 A	48.42	2.49	16.34	9.62	7.53	12.28	2.51	0.41	0.26	0.15	100.11
AHA27 A	49.37	3.25	14.81	11.19	6.07	11.29	3.01	0.50	0.34	0.15	100.00
AHA28 A	49.62	3.06	16.83	11.26	4.19	7.25	4.81	1.83	0.95	0.20	99.78
AHA29 A	48.66	2.98	15.83	10.50	6.78	11.52	2.77	0.47	0.32	0.18	100.19
AHA30 A	48.39	2.17	15.03	9.89	10.09	11.54	2.18	0.41	0.22	0.09	100.52
AHA31 A	48.17	3.70	16.46	11.60	5.37	8.41	3.97	1.42	0.73	0.16	99.65
AHA32 A	47.79	2.45	14.03	10.46	11.50	10.54	2.39	0.46	0.27	0.12	100.04
D12 A	48.82	3.43	14.07	12.06	6.44	11.08	3.08	0.51	0.35	0.16	100.40
D9 A	48.59	2.17	15.92	9.30	8.60	12.25	2.40	0.37	0.22	0.19	100.29

[a] Analytical techniques are described in the text. Reported total is as analyzed.

Table 4. Trace Element Analyses by ICPMS[a]

Sample	Sc	Cr	Co	Ni	Cu	Zn	Rb	Sr	Y	Zr	Nb	Ba	La	Ce	Pr	Nd	Sm	Eu	Gd	Tb	Dy	Ho	Er	Tm	Yb	Lu	Hf	Ta	Pb	Th	U
AHA18 A	29	496	68	176	76	81	5.3	308	20.7	116	14.9	68	9.83	23.57	3.38	14.92	3.89	1.32	4.06	0.65	3.81	0.77	2.05	0.28	1.69	0.24	2.80	1.64	0.77	0.93	0.33
AHA19 A	25	566	80	419	78	84	4.5	258	17.4	97	12.6	57	8.30	19.90	2.84	12.55	3.26	1.12	3.42	0.55	3.20	0.64	1.70	0.24	1.41	0.20	2.31	1.45	0.63	0.78	0.31
AHA20 A	32	290	70	95	87	99	7.5	377	28.5	173	22.3	98	14.47	34.56	4.92	21.54	5.50	1.84	5.68	0.90	5.21	1.04	2.75	0.38	2.27	0.32	3.95	2.09	1.07	1.33	0.42
AHA21 A	30	257	63	88	81	93	7.1	363	27.0	162	21.0	92	13.60	32.49	4.62	20.28	5.17	1.73	5.35	0.85	4.90	0.98	2.60	0.36	2.14	0.31	3.74	1.97	0.97	1.26	0.44
AHA22 A	30	486	71	225	78	97	6.8	353	25.0	147	18.9	86	12.42	29.66	4.23	18.52	4.73	1.61	4.93	0.79	4.59	0.91	2.43	0.34	2.02	0.29	3.41	1.72	0.95	1.15	0.39
AHA23 A	32	274	69	97	82	96	6.1	344	25.0	138	19.0	76	11.68	27.95	4.01	17.81	4.61	1.59	4.91	0.79	4.57	0.91	2.41	0.33	1.98	0.28	3.26	1.86	0.87	1.09	0.43
AHA25 A	28	675	77	316	64	83	4.5	332	18.5	102	13.9	59	8.64	20.81	2.98	13.20	3.43	1.21	3.62	0.58	3.39	0.68	1.82	0.25	1.51	0.21	2.41	1.49	0.68	0.79	0.28
AHA26 A	33	467	66	138	84	93	6.1	358	24.5	138	18.6	78	11.68	28.11	4.02	17.81	4.61	1.58	4.85	0.78	4.52	0.91	2.41	0.34	2.00	0.29	3.26	1.76	0.85	1.05	0.38
AHA27 A	37	120	80	60	100	116	8.6	364	33.0	196	26.1	110	16.58	39.61	5.63	24.80	6.37	2.11	6.63	1.06	6.09	1.21	3.21	0.44	2.64	0.38	4.57	2.45	1.12	1.52	0.57
AHA28 A	17	1	41	3	14	128	31.3	538	48.2	433	56.2	324	41.73	95.02	12.73	52.77	11.78	3.58	10.87	1.61	8.92	1.73	4.54	0.63	3.74	0.54	8.97	3.75	3.04	3.64	1.32
AHA29 A	34	241	65	84	84	107	7.6	356	30.6	176	23.2	99	14.78	35.31	5.05	22.26	5.73	1.91	6.01	0.96	5.56	1.12	2.94	0.41	2.44	0.35	4.10	2.07	1.00	1.33	0.40
AHA30 A	32	501	78	242	88	94	5.9	325	22.7	126	16.7	73	10.98	26.11	3.74	16.51	4.30	1.47	4.52	0.72	4.17	0.83	2.19	0.30	1.80	0.26	3.02	1.73	0.82	0.98	0.31
AHA31 A	22	13	60	29	27	127	25.2	561	41.6	350	47.9	271	35.14	79.68	10.80	44.96	10.27	3.19	9.65	1.43	7.78	1.50	3.88	0.53	3.16	0.46	7.55	3.42	2.48	2.88	0.98
AHA32 A	29	564	76	304	86	99	6.4	315	24.6	143	18.5	81	12.01	28.58	4.09	17.91	4.62	1.55	4.84	0.77	4.50	0.90	2.38	0.34	1.99	0.28	3.37	1.84	0.90	1.14	0.37
D11 A	44	462	67	316	105	109	5.9	308	27.5	141	19.5	75	11.31	27.63	3.98	17.86	4.81	1.65	5.16	0.84	4.99	1.01	2.70	0.34	2.29	0.33	3.36	1.30	0.76	1.00	0.32
D12 A	36	95	59	60	100	122	9.4	354	34.9	198	26.1	113	17.09	41.21	5.83	25.75	6.69	2.18	7.00	1.14	6.65	1.34	3.55	0.50	3.02	0.44	4.79	1.98	1.27	1.49	0.48
D14 A	39	129	47	59	116	127	10.5	367	37.3	227	28.6	138	19.95	47.07	6.72	29.19	7.46	2.39	7.59	1.22	6.81	1.39	3.65	0.52	3.01	0.45	5.26	1.87	1.24	1.83	0.59
D15 B	48	278	54	96	123	120	7.6	428	34.0	180	24.5	101	15.06	36.81	5.31	23.75	6.31	2.13	6.56	1.05	6.09	1.23	3.25	0.35	2.71	0.39	4.19	1.58	0.96	1.31	0.41
D15 C	43	97	54	75	137	125	8.3	358	33.5	193	27.6	103	15.98	37.80	5.35	23.31	5.89	1.96	6.11	0.95	5.81	1.16	3.06	0.42	2.47	0.36	4.28	1.61	1.02	1.47	0.45
D16 C	28	47	36	42	78	102	6.6	344	26.2	147	21.0	80	12.60	30.22	4.28	18.88	4.82	1.58	4.98	0.80	4.58	0.92	2.38	0.39	2.02	0.29	3.32	1.29	0.72	1.22	0.45
D20 A	31	862	92	688	84	107	5.5	253	21.4	119	16.2	71	9.86	23.20	3.29	14.52	3.76	1.24	3.84	0.61	3.77	0.76	1.97	0.27	1.61	0.24	2.66	0.94	0.62	0.88	0.28
D24 A	41	280	49	105	110	104	5.9	337	27.0	144	19.4	78	12.26	29.80	4.33	19.32	5.17	1.74	5.46	0.87	5.01	1.00	2.63	0.37	2.19	0.31	3.54	1.30	0.82	1.03	0.33
D25A	36	300	63	106	100	106	7.7	375	29.0	163	22.5	86	14.12	33.82	4.76	20.95	5.48	1.85	5.76	0.93	5.49	1.11	2.96	0.42	2.51	0.36	3.86	1.81	0.89	1.12	0.40
D25B	34	304	62	108	94	101	7.4	373	28.0	158	21.7	80	13.35	32.02	4.50	19.87	5.20	1.73	5.41	0.86	5.09	1.03	2.75	0.38	2.29	0.33	3.47	1.63	0.74	0.96	0.35
D27 A	26	113	46	78	41	113	15.7	532	32.1	225	31.3	187	23.13	53.80	7.50	32.21	7.82	2.53	7.54	1.14	6.21	1.20	3.09	0.43	2.49	0.36	5.38	2.01	1.68	1.75	0.58
D27 I	34	180	54	120	38	102	14.6	481	31.6	219	30.7	167	21.03	49.18	6.90	29.79	7.39	2.43	7.19	1.11	6.20	1.20	3.14	0.37	2.59	0.37	5.21	1.98	1.45	1.70	0.57
D28 A	42	288	48	94	98	102	6.6	339	29.1	156	21.1	87	12.87	31.28	4.54	20.24	5.38	1.85	5.73	0.92	5.34	1.06	2.83	0.35	2.37	0.34	3.74	1.38	0.79	1.15	0.36
D30 A	51	154	60	82	165	148	9.5	316	39.5	220	32.0	113	19.03	44.60	6.42	28.27	7.29	2.32	7.71	1.23	7.22	1.45	3.89	0.41	3.30	0.47	5.19	2.11	1.38	1.69	0.55
D30 D	36	102	46	53	136	135	9.2	293	36.1	207	30.1	110	18.73	43.98	6.36	27.84	7.17	2.22	7.45	1.18	6.78	1.37	3.61	0.51	3.02	0.43	5.10	2.06	1.19	1.68	0.53
D31 A	38	78	51	58	126	137	9.2	324	37.5	210	31.6	116	18.91	45.05	6.46	28.31	7.34	2.37	7.47	1.19	6.81	1.36	3.59	0.42	2.97	0.42	4.91	2.02	1.22	1.78	0.58
D33 B	50	272	53	89	98	95	7.0	376	30.7	168	23.7	95	14.79	36.03	5.23	23.26	6.20	2.11	6.50	1.05	6.13	1.22	3.22	0.36	2.67	0.38	4.29	1.64	1.00	1.47	0.53
D33 C	43	314	43	75	80	77	5.7	300	25.2	138	19.3	75	11.76	28.55	4.15	18.52	4.94	1.70	5.30	0.85	5.00	1.01	2.64	0.34	2.23	0.32	3.60	1.36	0.76	1.15	0.39
D35 A	16	3	23	4	12	159	38.6	597	68.9	476	76.3	428	57.79	134.79	18.61	78.94	17.69	5.13	16.05	2.35	12.66	2.43	6.29	0.64	5.05	0.73	10.04	4.46	3.33	4.04	1.30
D9 A	30	480	57	167	83	85	5.8	334	21.3	118	15.4	72	10.57	25.44	3.60	15.89	4.16	1.43	4.39	0.71	4.18	0.84	2.23	0.31	1.88	0.28	2.94	1.44	0.96	0.90	0.31
W-2	36	93	45	72	103	73	20.3	190	22.4	88	7.7	167	10.54	22.71	3.01	12.65	3.31	1.08	3.64	0.62	3.87	0.82	2.29	0.34	2.09	0.31	2.31	0.48	7.65	2.12	0.50
RSD%	4.4	4.0	4.1	3.4	4.6	5.2	4.7	2.0	2.5	2.8	1.7	1.3	2.7	2.7	2.1	2.2	2.7	2.6	3.2	3.1	2.7	3.0	2.7	3.8	3.3	3.8	2.2	3.0	2.8	2.9	4.4

[a] Analytical techniques described in text. Analysis of standard W-2 is reported, as well as estimated precision based on replicated analyses.

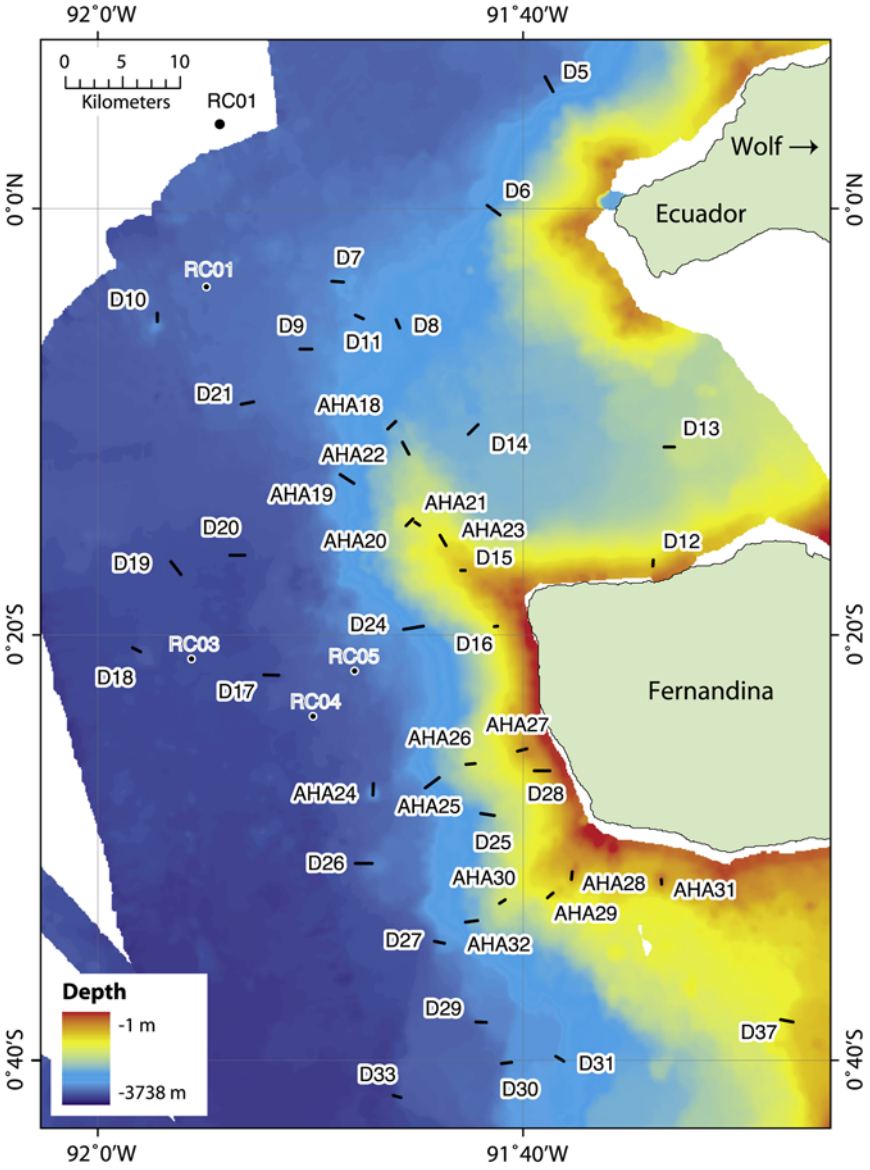

Figure 3. Dredge and wax-core locations superimposed on detailed bathymetric map of submarine Fernandina. The southwest, west, and northwest rift zones appear as sharp ridges emanating from the coastline.

local and regional slopes and morphology, as determined with multibeam data (Figures 2 and 4). The side-scan sonar data are especially important in the deep-water area west of Fernandina, where we observe acoustically distinct lava flows that do not appear in bathymetry records.

3.1. Submarine Rift Zones

[10] Side-scan images (Figures 1 and 2) have been inverted so that dark represents high backscatter and light is low backscatter or acoustic shadow. Highly reflective, mottled terrain predominates on submarine ridges that extend radially southwest, west, and northwest of Fernandina (Figure 4). The northwest and southwest submarine ridges are aligned with diffuse subaerial rifts identified by *Chadwick and Howard* [1991]. Identification of craters and small cratered cones and the recovery of fresh pillow basalts indicate that these features are active submarine rift zones that extend the active volcanic province of Fernandina over 30 km beyond the coastline. The morphology of the submarine rift zones is different from that of the subaerial sectors, with steeper along-axis and across-axis slopes. The northwest submarine rift is ~30 km long and ~8 km wide. Its average

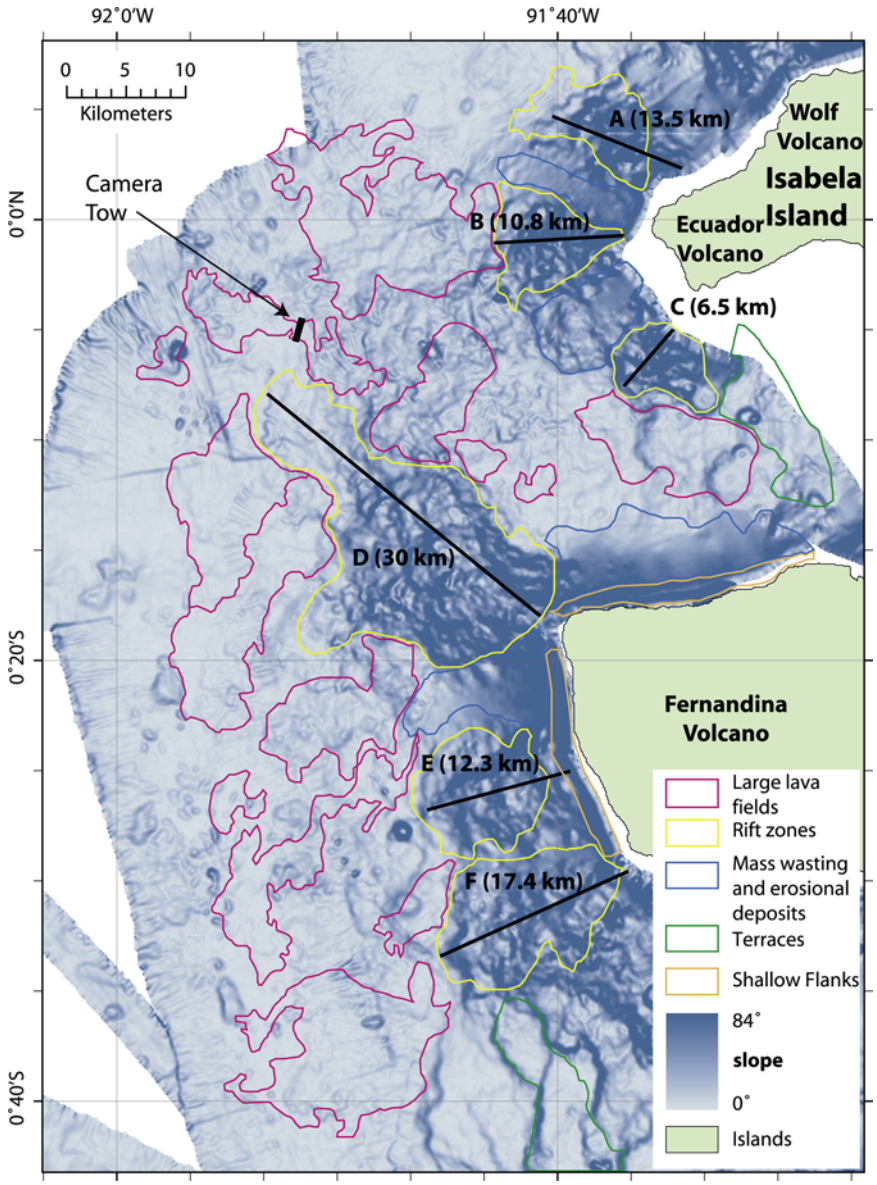

Figure 4. Slope map of the seafloor west and north of Fernandina (darker shades are steeper slopes; see key) based on multibeam data, with geologic interpretation from Figure 2 overlain. Locations of topographic sections along rift zones (Figure 5) and lengths (in parentheses) are noted, as is the location of the camera tow discussed in the text.

gradient is 161 m/km (Figures 4 and 5), compared to 73 m/km for Kilauea's Puna Ridge [*Smith et al.*, 2002] and 43 m/km for Genovesa Ridge [*Harpp et al.*, 2003]. The western submarine rift zone differs from the northwest and southwest submarine rifts in that there is no concentration of subaerial vents on this sector of the volcano's flank. The submarine expression of the western rift is, however, well defined, and both its acoustic texture and its slopes are similar to the northwest and southwest submarine rifts.

3.2. Large Deep-Water Lava Fields

[11] The second acoustic facies observed in the side-scan data consists of large (~5–30 km^2) irregularly shaped areas of higher reflectivity at depths >3000 m west and northwest of Fernandina. On the basis of comparison with mid-ocean ridge side-scan images and digital photographic data collected during the DRIFT4 cruise, these large areas are identified as lava fields comprising pillow, sheet, and lobate flows with variable sediment cover emplaced on flat seafloor. The western part of the terrain is characterized by slopes of <5 m/km,

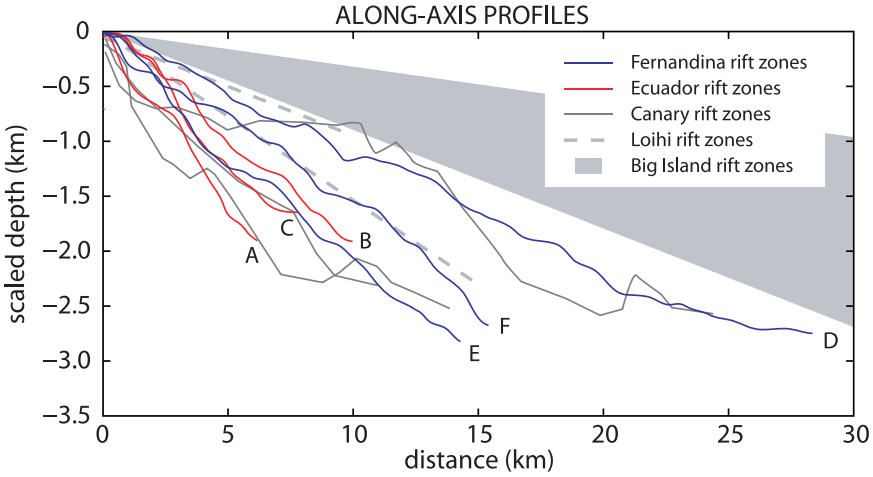

Figure 5. Topographic profiles along submarine rift zones offshore Fernandina and Ecuador volcanoes as shown in Figure 4, compared to rift zones at Hawaii, Loihi, and the Canary Islands.

and the eastern part by slopes of ~20 m/km. The planar dimensions of individual flow fields range up to about 20 km long and between 1 and 8 km wide.

[12] Eruptive vents for the large lava fields are difficult to discern on side-scan images, although the proximity of these flows to the distal parts of the submarine rifts of Fernandina and the west submarine rift of Ecuador volcano on Isabela suggests that many of the lava fields erupted from the rifts (Figures 1 and 2). Recently collected 30 kHz EM300 multibeam data, which have four times the resolution of our multibeam grids, confirm the presence of numerous vents that are likely sources for the deep-water lava flows (J. Glass et al., Submarine volcanic platform building in the western Galápagos Archipelago: Observations from EM300 bathymetry and MR1 side-scan sonar, submitted to *Geochemistry, Geophysics, Geosystems*, 2006). The lava flow fields differ in the strength of their reflectivity, probably because of variable sediment cover. In a few cases, the younger flows include isolated patches of lower reflectivity, probably kipukas of older terrain. Images from a camera tow over one of the large lava flows (Figure 4) extending northwest from the deeper part of Fernandina's northwest submarine rift show that 45% of its surface is covered with sediment thick enough to obscure the surface morphology. Otherwise, the flow tops consist of 42% pillows, 12% sheet morphology, and <1% lobate lavas. Photographs and 12 kHz pinger records suggest that the flow is likely to be <5 m thick. The uniformity of sonar reflectivity across many of the flows and our interpretation of seafloor digital images suggest that the large lava flows are likely to be compound flow fields that may have formed during single eruptive episodes.

3.3. Shallow Submarine Flanks

[13] The upper 1200 m of the west and north submarine flanks of Fernandina are made up of dozens of finely layered reflectors, each several kilometers long (Figure 2). These layers appear to be subaerial lava flows that crossed the coastline and have since been truncated by wave erosion and slumping in the shallow coastal areas, producing unstable clastic deposits on over-steepened slopes. No reef or wave-cut terraces are apparent in the side-scan data in these areas; hence there is no clear measure of subsidence.

3.4. Mass-Wasting and Erosional Deposits

[14] Gravitational slumping is known to be an important process on Hawaiian shields and other oceanic islands and plays a formative role in their development [e.g., *Fornari and Campbell*, 1987; *Lipman et al.*, 1988; *Moore et al.*, 1989; *Lenat et al.*, 2001; *Normark et al.*, 1993]. Fernandina lacks evidence for large-scale flank slip or sector collapse, despite its unbuttressed western flank.

[15] The north submarine flank of Fernandina and one area on the west flank have smooth and steep slopes, moderate to low backscatter amplitude, and east-west trending lineations in the sonar imagery, all suggestive of small-scale mass wasting and down slope transport of volcanogenic sediment from erosion of the coastline and gravitational slides (Figures 2 to 4). The talus apron on the northern slope of Fernandina extends laterally from the northwest submarine rift to the northeast corner

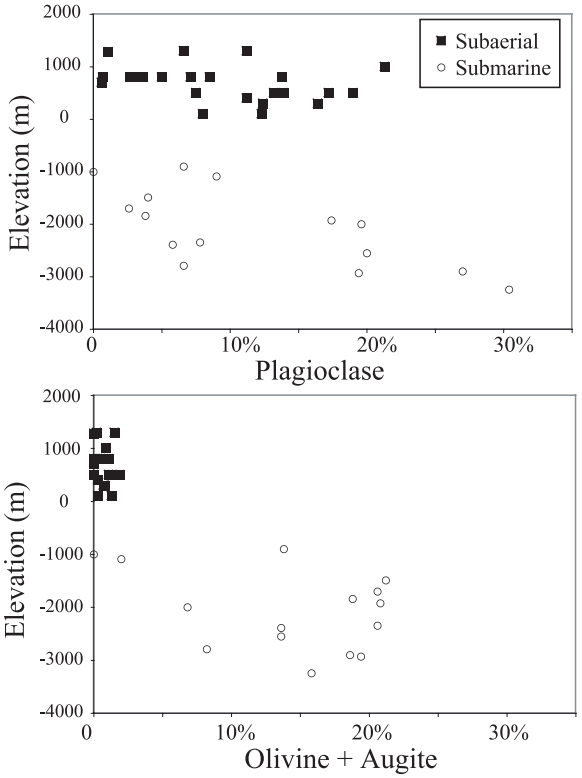

Figure 6. Modes of submarine (open circles) and subaerial lavas (black squares) (subaerial data from *Allan and Simkin* [2000]). Criteria for plagioclase phenocrysts are those >0.5 mm in long dimension. Mafic phenocrysts are defined as being >0.3 mm in diameter.

of the island at 1200 m to 2100 m water depth. As on the west flank, there is no evidence of sector collapse on the northern slope. The dominance of talus and lack of lava in this sector of the volcano indicate an absence of young eruptive vents; likewise, there are few subaerial vents on the northern flank of Fernandina [*Chadwick and Howard*, 1991; *Rowland*, 1996].

3.5. Submarine Terraces

[16] In the submarine region between Fernandina and Cerro Azul volcanoes (Figure 2), at least six large, stacked terraces up to ~140 km^2 in area decorate the seafloor. Each terrace is bound on its upper and lower sides by steep escarpments, and its top is flat. The bounding escarpments are scalloped, with convex-out lobes 100–1000 m across. There is no sign of mass-wasting deposits downslope from the layered escarpments. The terrace lavas have a clear geochemical affinity to Fernandina (Tables 2 to 4). These terraces are similar in morphology to terraces that define the southern margin of the Galápagos platform south of Isabela [*Diefenbach*, 2005] (Figure 1). The Cerro Azul and Fernandina terraces are interpreted to be thick sequences of large-volume lava flows that mark major eruptive phases in the construction of the southwest Galápagos platform.

4. Lava and Glass Compositions

[17] The most prominent petrologic feature of Fernandina's submarine lavas is that they contain up to 20% olivine and augite phenocrysts together with platioclase (Figure 6), in marked contrast to the subaerial lavas, which only contain sparse olivine and are dominated by plagioclase phenocrysts [*Allan and Simkin*, 2000]. Fernandina's submarine glasses fall into three compositional groups (Figures 7 and 8). The majority of the glasses have 5.0 < MgO < 7.6%, define coherent trends on variation diagrams, and have 0.38 < K_2O < 0.77% (Figure 7); we refer to these rocks as the "normal series". Normal-series glasses have compositions similar to aphyric subaerial lavas [*Allan and Simkin*, 2000]. A second population of glasses forms an "evolved series" with 3.19 < MgO < 5.0% and K_2O > 1.5% and include icelandites. Samples from D27 (Figure 3) define a third "high-K series"; these have MgO contents that overlap the normal series but with elevated K_2O (> 1.0%; Figure 7). The normal-series lavas are by far the dominant basalt type in all of Fernandina's submarine eruptive units, whereas all of the evolved series and the high-K lava (D27) erupted from the southwestern sector of the volcano (Figure 3). Sulfur concentrations in the glasses range from 0.01 to 0.18 wt.%, and there is no relation between sulfur concentration and the depth at which the sample was collected (Table 2). Comparison of glass and whole-rock compositions of the same samples reveals little overlap in their major element compositions (Table 3 and Figure 9).

[18] Rare earth element (REE) patterns and incompatible trace element abundances of normal-series basalts are similar to those of the subaerial basalts analyzed by *Allan and Simkin* [2000] (Table 4 and Figure 10). Although all are light REE enriched they have depletions in the most incompatible elements (Rb, Ba, and Th). Fernandina lavas have high concentrations of Nb and Ta (Figure 11) [*Kurz and Geist*, 1999] and low Nb/Ta: average Nb/Ta for Fernandina is 9.5, compared to 17.5 for most other mantle-derived rocks [*Green*, 1995]. Both positive and negative Sr anomalies are apparent in the normal-series lavas. The heavy rare earth elements have steep negative slopes (Figure 10).

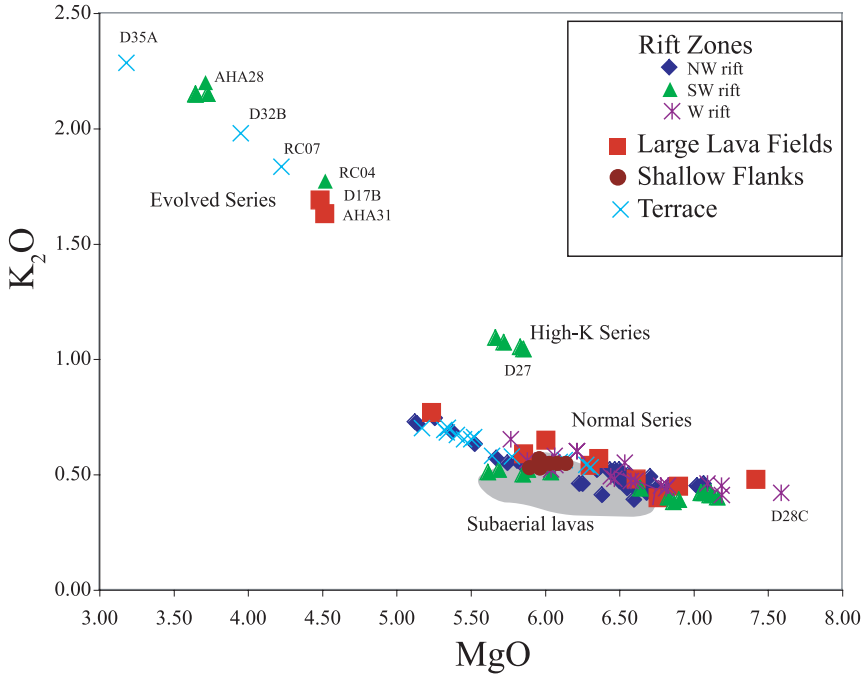

Figure 7. MgO versus K_2O for Fernandina submarine glasses and subaerial rocks indicating compositional differences between normal, evolved, and high-K series, and comparison to subaerial suite of *Allan and Simkin* [2000]. Geologic units are as described in text.

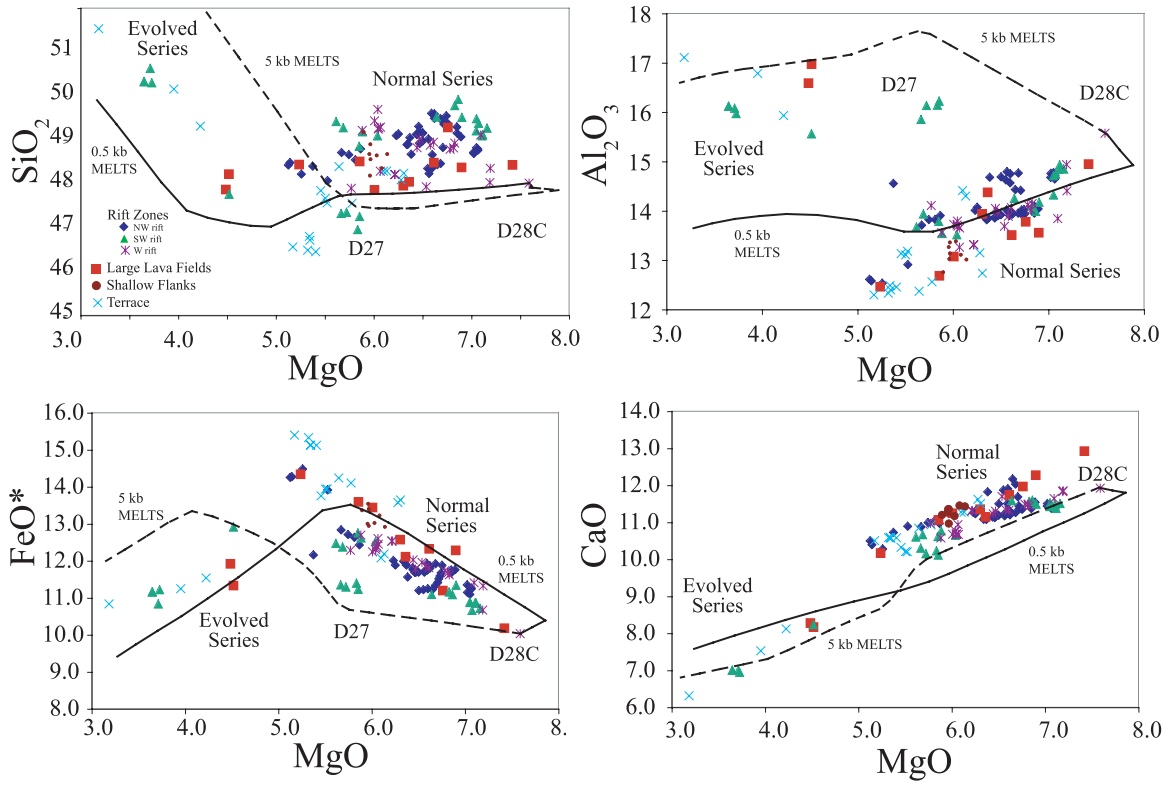

Figure 8. Major element variation diagrams for Fernandina submarine glasses, compared to modeled liquid-lines-of-descent from MELTS, run at 500 b and 5 kb. Symbols are the same as in Figure 7.

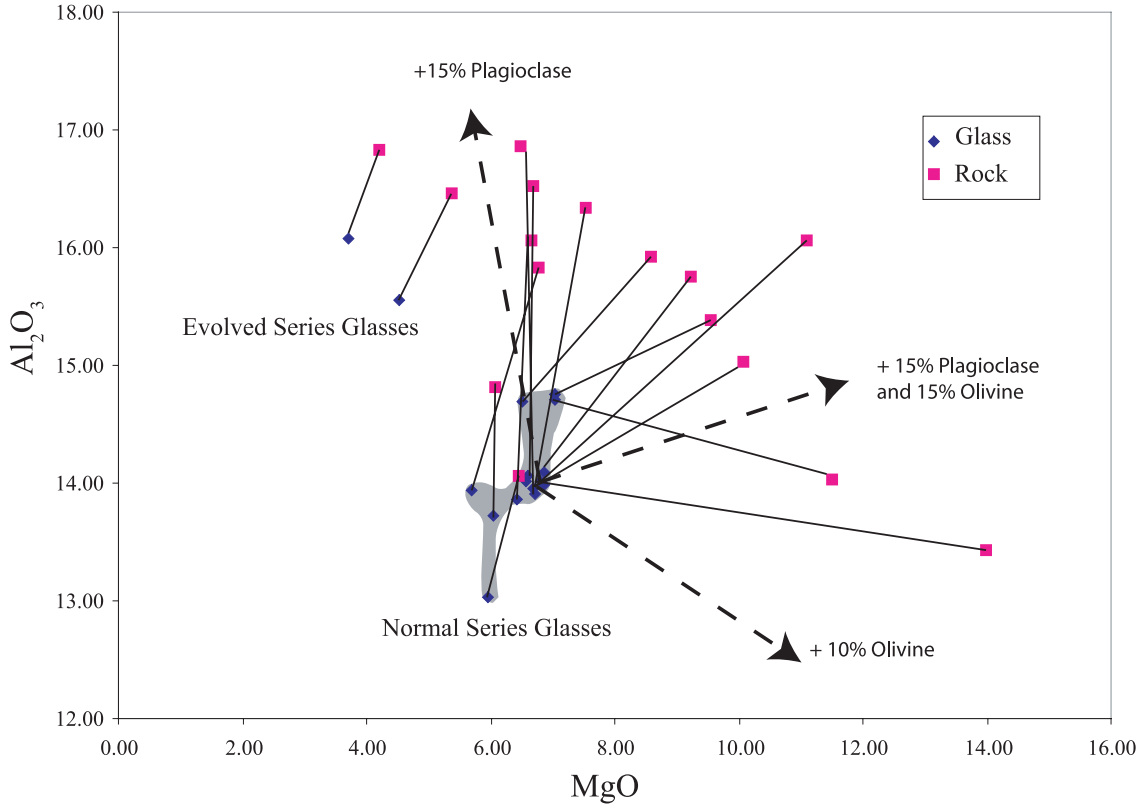

Figure 9. Comparison of whole rock and glass compositions. Tie lines connect pairs of rock and glasses from the same sample. Shaded field encompasses normal series glasses. Vectors indicate the compositional effects of adding variable amounts of plagioclase and olivine to the glasses.

[19] The evolved series lavas have slightly steeper REE slopes than the normal series (Figure 10) and pronounce negative Sr anomalies. Otherwise, they have patterns that are parallel to the normal series and subaerial lavas, with nearly equal enrichment of the incompatible elements. The high-K series lava (D27A) has La/Sm and Sm/Yb ratios intermediate between those of the normal and evolved series.

[20] One goal of the submarine sampling was to obtain lavas from older stages of growth of Fernandina because the subaerial volcano has been completely resurfaced in the past few millennia [*Kurz et al.*, 2005]. All of the samples collected from steep submarine flanks that could represent older parts of the volcano (e.g., D12, D25, D28, Figure 3) belong to the normal series and have compositional characteristics that are indistinguishable from historically erupted lavas [*Allan and Simkin*, 2000].

[21] Samples D9 and RC01 were collect about 9 km apart from a 20-km long flow field to the northwest of Fernandina (Figure 2). These glasses are nearly identical in composition (wt.% MgO = 6.7 versus 6.5; K_2O = 0.45 versus 0.45; S = 0.14 versus 0.15). Two more samples, D17 and RC04, were collected about 5 km apart across the flow direction of a 20-km long flow directly west of Fernandina. No rocks were retrieved in D17; instead, a compositionally heterogeneous population of glasses was found in the burlap sack tied to the dredge bag. One of these glasses has a composition identical to RC04 glass. These results are consistent with the interpretation of sonar data as indicating individual flow units, although far more samples are needed to rigorously test this.

5. Mineral Chemistry

[22] Olivine phenocrysts in a subset of eight submarine rocks range from Fo_{72} to Fo_{89}, which compares to the range in subaerial phenocrysts of

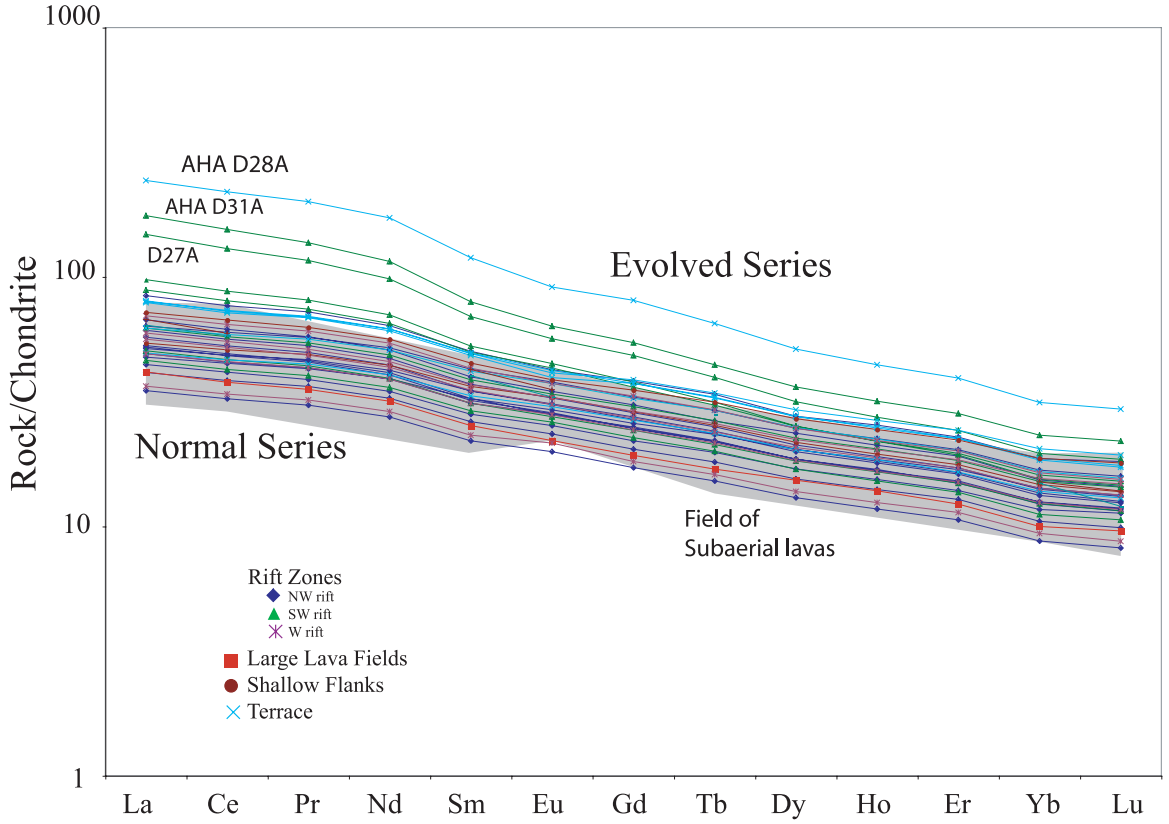

Figure 10. Chondrite-normalized REE diagram of submarine Fernandina lavas (Table 4) compared to field for subaerial rocks (from *Allan and Simkin* [2000]). Note that subaerial lavas are analyzed for a slightly different suite of elements than the submarine lavas (La, Ce, Sm, Eu, Tb, Yb, and Lu only). Symbols as in Figure 7. *Sun and McDonough* [1989] is the chondrite normalization.

Fo_{76-85} [*Allan and Simkin*, 2000] (Figure 12). The cores of all analyzed olivines are more forsteritic than predicted if they were in equilibrium with the host glasses, although phenocryst rims in some grains approach equilibrium values (Figure 12). Zoning profiles in eight olivine crystals from sample AHA29A (MgO = 5.69%) are representative of the olivine populations in all of the normal-series lavas and indicate at least four populations of olivine (Figure 13). Sample AHA29A glass is in equilibrium with Fo_{77}. Three of the olivines have cores with constant compositions of $\sim Fo_{83}$ and have thin, normally zoned rims. One grain is more forsteritic (Fo_{86}) and unzoned. Two grains have cores that average Fo_{81}, and one grain is irregularly zoned, with sectors whose compositions are like those in the previous two types.

[23] Plagioclase phenocryst compositions range from An_{49} to An_{96}, and there is no relation between the crystals' compositions and the composition of their host glass. Most grains have large cores with major changes in composition (>10% An) across $\sim$10 microns, whereas some grains have normally zoned rims.

6. Discussion

6.1. Submarine Rift Zones

[24] The western Galápagos volcanoes have been considered an end-member of basaltic volcano morphology and construction, owing to their radial symmetry and the lack of focused rift zones on the subaerial edifice [*McBirney and Williams*, 1969; *Chadwick and Howard*, 1991]. In contrast to its subaerial sectors, the submarine slopes of Fernandina are dominated by three volcanic rift zones. Fernandina's northwest submarine rift occupies an area of $\sim$310 km^2, whereas the other two submarine rifts are $\sim$88 km^2 and 129 km^2 (Figure 2). Cumulatively, the rift zones nearly equal the subaerial area of Fernandina of about 640 km^2.

[25] There is no evidence that the orientations of Fernandina's submarine rift zones (or those of any

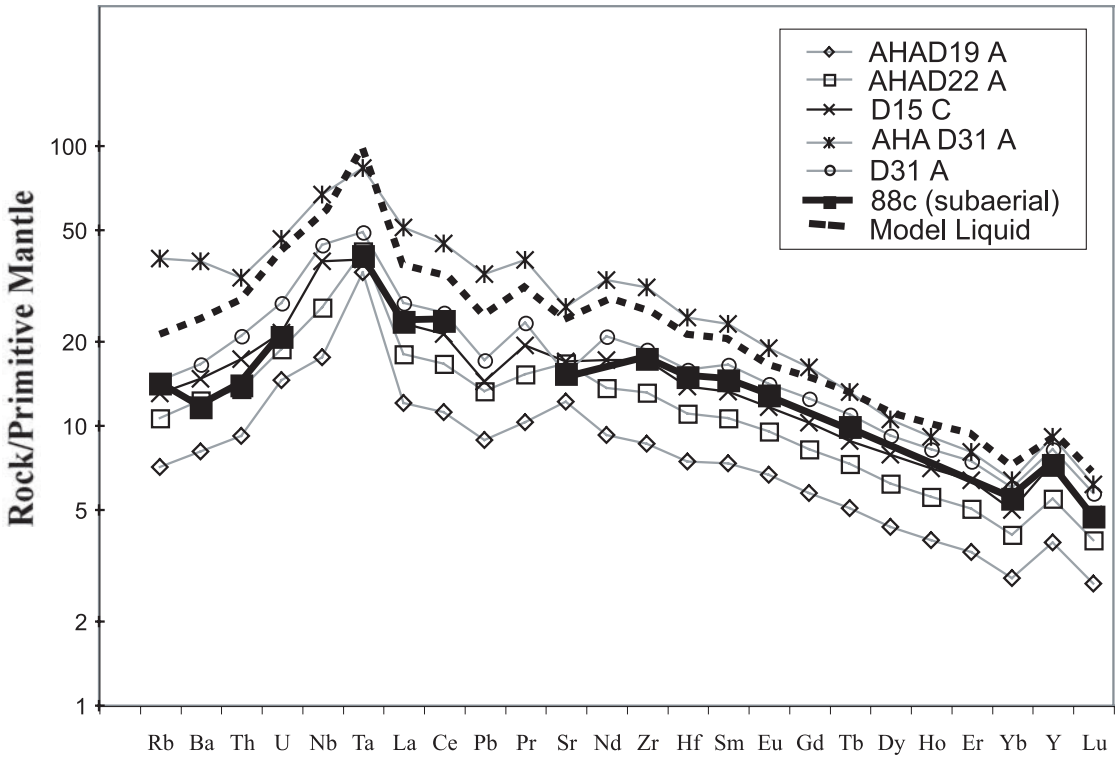

Figure 11. Trace element diagram of representative Fernandina submarine lavas, normalized to primitive mantle values of *Sun and McDonough* [1989]. A representative subaerial rock from *Allan and Simkin* [2000] (sample 88c) is shown for comparison. AHA 31A is an evolved-series lava. See Figure 3 for sample locations. "Model liquid" is calculated pattern after 58% fractional crystallization of an assemblage consisting of 68% augite, 27% plagioclase, and 5% magnetite; melt fraction and mode are from 5 kb MELTS run, with the details in the text. Parental magma is sample AHA26A (7.53% MgO).

of the other western volcanoes) are controlled by regional tectonic stresses. The rift zones are not parallel to any other regional structure (i.e., the GSC, the 91° transform, absolute plate motion, or the Wolf-Darwin or other tectonic lineaments; Figure 1). The submarine rift zones at Fernandina, Wolf, Cerro Azul, and Ecuador volcanoes do, however, form a consistent pattern where they are oriented away from the next nearest, older volcano (Figure 1). Fernandina's rifts, for example, point away from Darwin and Alcedo volcanoes. These orientations are likely due to buttressing effects of the neighboring volcanoes, and possibly also to stresses developed by lithospheric loading. In Hawaii, most of the rift zones are oriented across the slope of the next-oldest volcano, owing to the tensional forces exerted by the sloping surfaces [*Fiske and Jackson*, 1972]. The exception is Loihi, whose south rift is oriented away from Kilauea [*Fornari and Campbell*, 1987], probably because Loihi has just begun to coalesce with Kilauea, and the slope forces are not yet significant [*Garcia et al.*, 2006]. In this regard, the Galápagos submarine rifts are most similar to those of Loihi.

[26] The strong side-scan reflectivity of Fernandina's submarine rift zone terrains and the fresh, glassy lavas indicate a young age. Seafloor sedimentation rates in the Galápagos region, away from any of the subaerial volcanoes, have ranged from 4 to 9 cm/ky for the past 130,000 y [*Lea et al.*, 2006], and the rates are certainly higher closer to the islands. Thus the submarine lava exposures on Fernandina's rift zones must be younger than a few thousand years. The resolution of our side-scan data does not permit identification of most of the vents on Fernandina's northwest rift, but the uni-

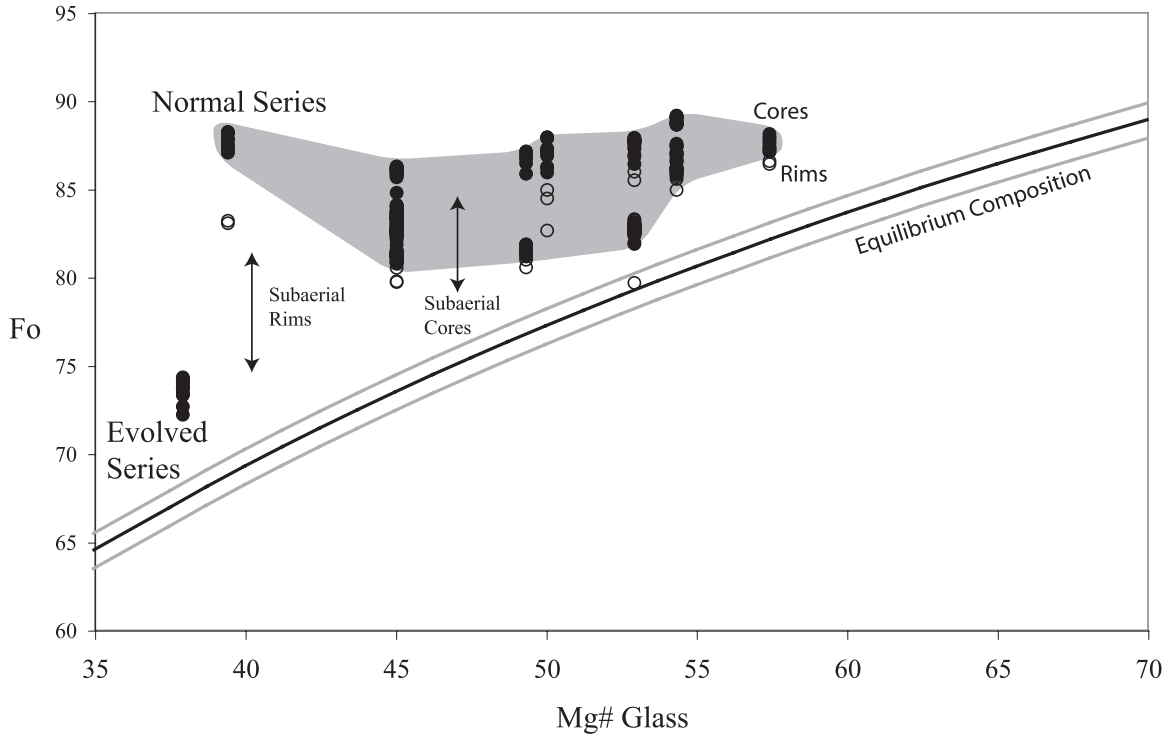

Figure 12. Mg# of host glasses versus Fo content of olivines. Curved bands indicate composition of olivine in equilibrium with the glasses, assuming that $(MgO/FeO)_{liquid}/(MgO/FeO)_{olivine}$ = 0.27 to 0.33 and that 10% of the iron in the liquid is ferric. The Mg# of the subaerial glasses are unknown, but forsterite contents from *Allan and Simkin* [2000] are shown.

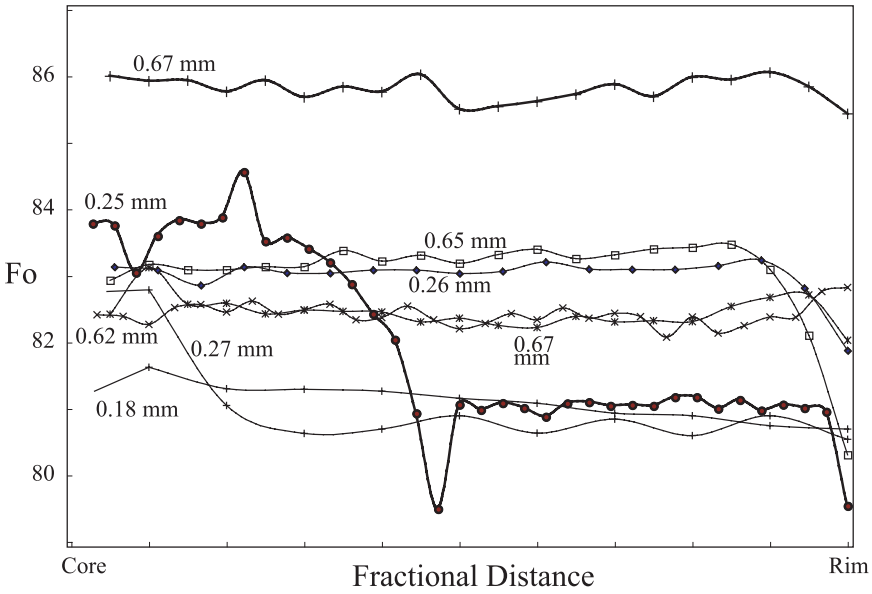

Figure 13. Zoning profiles across eight olivine phenocrysts in sample AHA29A (MgO = 5.69%), a typical normal series lava. The glass of sample AHA29A is in equilibrium with Fo_{77}. Olivine grains are coarse crystals from crystalline interiors of samples. The radius of each crystal is indicated.

form hummocky acoustic texture and strong backscatter (Figure 2), as well as small cones and craters (Figure 3), point to low effusion rate (pillow lava) eruptions along the rift's summit and perhaps from its flanks.

[27] Fernandina's submarine rifts are similar in gross morphology to rifts on other ocean island volcanoes, such as those on Loihi [*Fornari et al.*, 1988; *Garcia et al.*, 2006] and Canary Island volcanoes [*Acosta et al.*, 2003]. They are dissimilar, however, to the archetypal Puna Ridge [*Fornari et al.*, 1979; *Holcomb et al.*, 1988; *Clague et al.*, 1995; *Lonsdale*, 1989; *Smith et al.*, 2002], which has steeper across-axis slopes and a shallower along-axis gradient. The lower subaerial flanks of Fernandina have an average slope of 4% [*Mouginis-Mark et al.*, 1996], whereas the submarine rift has an axial slope of 11% (Figure 5).

[28] Steepening from the subaerial to submarine edifice is common to most ocean island rift zones [*Fialko and Rubin*, 1999]. Models of rift zone formation indicate that the along axis slope may be controlled by the dimensionless group, $\Delta\rho/\rho_{(a\ or\ w)}$, where $\Delta\rho$ is the density difference between the magma and host rock, ρ_a is the density difference between magma and air ($\rho_a \cong \rho_{magma}$), and ρ_w is the density difference between magma and water [*Fialko and Rubin*, 1999]. The difference in relative magma density ($\rho_a > \rho_w$) between the subaerial and submarine rift is likely responsible for the steepening of Fernandina's rifts at the coastline.

[29] The paradox of Fernandina's submarine rift zones is that they form sharp ridges, indicating that the eruptive centers are focused, whereas the subaerial flanks of the volcano are characterized by diffuse radial venting and a broad topographic profile. The diffuse radial rifts of the NW and SW subaerial sectors of Fernandina, as well as historical evidence of sill intrusion and dipping dikes into the flanks of the volcano [*Cullen et al.*, 1987; *Jónsson et al.*, 1999], indicate that the deviatoric stresses are small and that the least compressive stress can be oriented subvertically in the volcano flanks (Figure 14). These features contrast with the Hawaiian shields, which grow on the flanks of the next-youngest volcano, and where strong gravitational stresses on the topographic slopes [*Fiske and Jackson*, 1972] and sliding on decollements [*Dieterich*, 1988] produce large deviatoric stresses, vertically oriented dikes, and as a result, focused rift zones. It follows that the steeper the across-axis topographic slope, the more likely vertically oriented dikes will be repeatedly injected in a narrow zone.

[30] *Chadwick and Dieterich* [1995] attributed the diffuse radial dikes on the subaerial flanks and the prominence of circumferential vents at the volcano summit to stresses induced by the subcaldera magma body. The pressurized magma body produces circumferential tensional stress near the summit, but tensional stress becomes radial outward on the flanks. The transition zone between these two stress regimes may be a location of weak deviatoric stress and promote the formation of diffuse subaerial rifts, whereas submarine rifts reflect the full development of the tangentially oriented tensional stress. We view the submarine rift zones at Fernandina as being the result of a positive feedback system, wherein the larger they grow and the steeper they get, the more likely the ridges are to focus laterally injected dikes.

[31] How does this positive feedback originate? At a small scale, differences in flow type are important. Submarine rifts are composed primarily of pillow flows, which do not spread as extensively as comparable subaerial flows and will tend to produce steeper constructional features. However, rifts are composed of hundreds of flows, and we expect that the effects of flow type on topography diminish with time. Instead, we suggest that the submarine rifts are more focused than the diffuse subaerial rifts because the regions between the subaerial rifts are filled in topographically by lavas erupted from the circumferential fissures near the summit. Lava flows erupted from the Fernandina's summit do not travel great distances beyond the coastline, thus they do not contribute to the construction of the submarine edifice. These in-filling lavas buttress the terrain between subaerial rift zones, diminishing topographically generated stresses and promoting diffuse radial venting. This model can explain the diffuse radial venting on the flanks of the volcano, the focused rifting on the submarine flanks, and the transition between the two modes at the coastline.

6.2. Large Lava Flow Fields

[32] Another attribute of submarine Fernandina is the presence of large-area deep-water lava flow fields to the west of the volcano. The deep-water lava flow fields northwest and west of Fernandina have areas ranging from $\sim$172 km^2 to $\sim$7 km^2 (Figure 2). In many cases, the large flow fields offshore from Fernandina can be traced to a source on the middle to lower flanks of the northwest

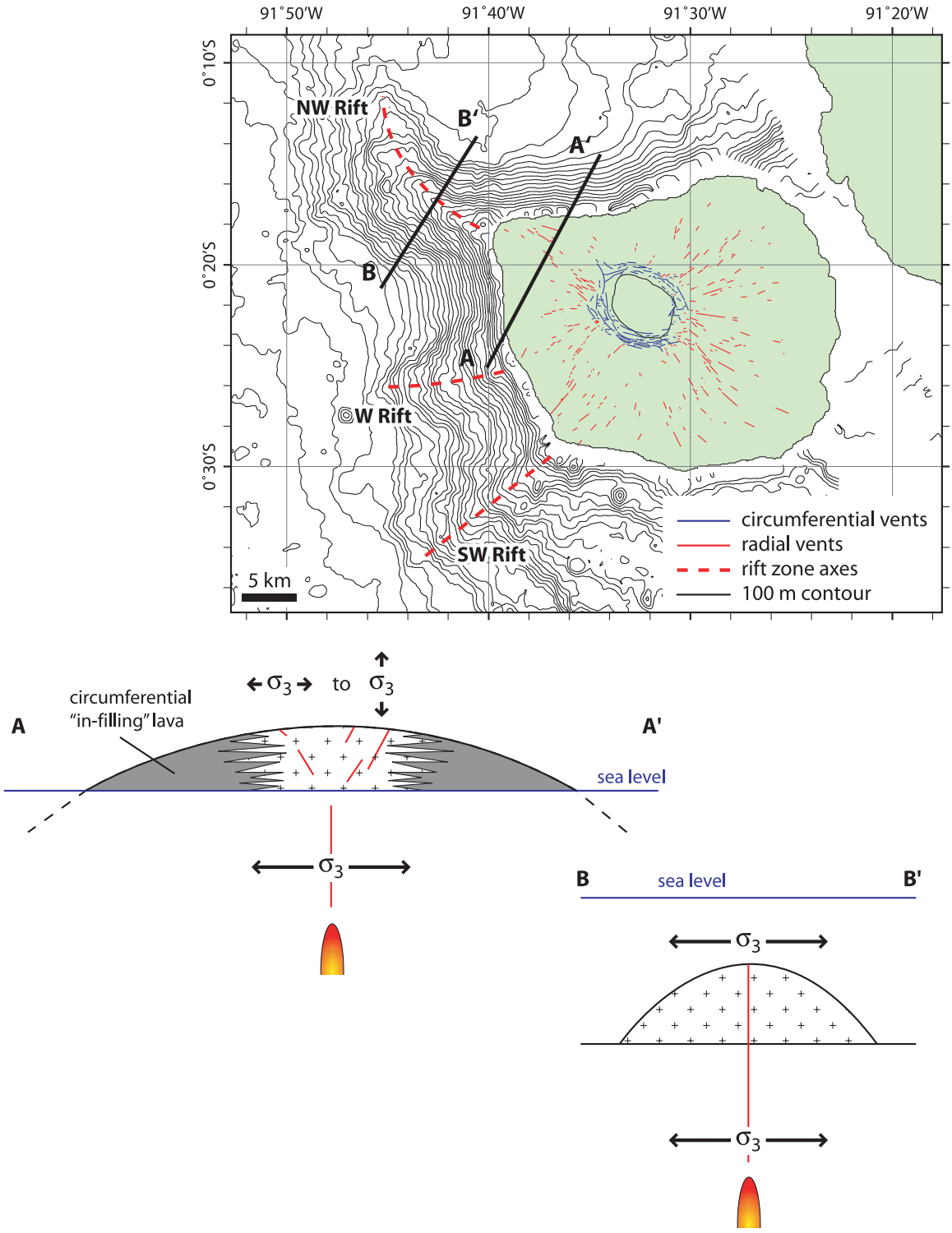

Figure 14. (top) Map of Fernandina Volcano showing the location of circumferential and radial fissures on the subaerial volcano [*Chadwick and Dieterich*, 1995] and submarine rift zones identified by this study. (bottom) Schematic cross section of the NW flank of the volcano. Maximum tensile stress (σ_3) is oriented normal to the radial direction and is larger at depth than in the shallow edifice. Large σ_3 results in focused dike intrusions at depth within the edifice. Low σ_3 reflects buttressing by "in-filling" lava flows from circumferential vents (dark gray). (bottom) Schematic cross section through the submarine NW rift zone. Maximum tensile stress is again oriented normal to radial and is as strong in the shallow crust as it is deep, resulting in focused rifting.

submarine rift, or the distal ends of the other rift zones including one extending west from Ecuador volcano. On the basis of one camera tow on the young flow field at the end of Fernandina's northwest rift (Figure 2), most of the flow has a pillow surface and little sediment cover; the flow thickness appears to be only a few meters. These flow fields have predominantly pillow morphology, suggestive of low effusion rates, yet some can be as long as ~20 km. If these submarine flow fields average 5 m thick and vesicles are neglected, then their volumes range from 0.04 to 0.9 km^3. In comparison, subaerial eruptions from Fernandina in 1988, 1991, and 1995 have a combined volume of 0.05 km^3, and the largest young subaerial flow has an estimated volume of 0.12 km^3 [*Rowland*, 1996]. Thus it appears that some submarine eruptions may be more voluminous than their subaerial counterparts. *Gregg and Fornari* [1998] theorized that such long lava flows are feasible on the seafloor over low slopes, but they are apparently rare. As far as we know, none has been observed on the flanks of Kilauea, Mauna Loa, or the Canary Islands. Well-mapped lava flow fields on the East Pacific Rise and Juan de Fuca Ridge only range from 0.03 to 55 km^2 [*Perfit and Chadwick*, 1998]. Lava flow fields of the North Arch offshore Hawaii lie 100 to 400 km north of Oahu, and one of the largest flows there is believed to be ~108 km long and 2 km wide and was emplaced on seafloor with a slope of ~0.1° [*Clague et al.*, 2002]. Additional deep-water lava flows have been mapped using GLORIA side-scan sonar along the Hawaiian chain [*Holcomb et al.*, 1988].

[33] The large Fernandina submarine lava flows have compositions that are indistinguishable from Fernandina's normal-series and subaerial lavas (Figures 7 to 11), suggesting that they form by lateral injection of magma from up to ~30 km from the volcano's central plumbing system. The larger volumes of these flows may result from an increased driving pressure, because the upper part of the magma chamber is elevated compared to the depth of the vents. Lavas erupted from circumferential fissures at the summit of the volcano require enough pressure to drive the magma upward through about 2800 m of low-density rocks, resulting in low-volume eruptions. Subaerial radial fissure vents are ~1000 m lower than the summit fissures, thus have a stronger driving force during eruption [*Rowland*, 1996; *Naumann and Geist*, 2000]. This hypothesis could be tested by further high-resolution mapping and in situ sampling of these large lava flows [cf. *Soule et al.*, 2005].

[34] We believe these deep-water, large-area flows represent the initial volcanism that will eventually coalesce to form a new extension of the Galápagos platform and the infrastructure of the next volcano at the leading edge of the Galápagos hot spot, west of Fernandina (Figure 15). The large lava flows are initially made from magmas that are injected laterally from the nearest volcano's magmatic plumbing system, and they stack and form terraces like those between Cerro Azul and Fernandina (Figure 1). The terraces then coalesce and form the plateau-like Galápagos Platform, with a base level of about −1000 m. Once the platform is constructed, the magma plumbing system centralizes, and the next discrete shield volcano forms, along with its submarine rift zones.

6.3. Petrologic Origin of the Normal Series

[35] Fernandina's subaerial lavas are remarkable for their compositional homogeneity [*Allan and Simkin*, 2000]. This homogeneity includes parameters that depend on temperature and extent of differentiation (e.g., Mg# = 0.52 ± 0.02) and ratios that are controlled by melting and source heterogeneity (e.g., K_2O/TiO_2 = 0.15 ± 0.01; Zr/Y = 5.9 ± 0.3). The only notable variations relate to Al_2O_3 and Sr, which have been attributed to plagioclase accumulation [*Allan and Simkin*, 2000].

[36] Liquid lines of descent have been calculated using the MELTS algorithm to test whether the normal series glasses might be related to each other by fractional crystallization (Figure 8) [*Ghiorso and Sack*, 1995]. The parental liquid is assumed to have a starting composition of the glass in D28C (7.59% MgO) and 0.3% water. Crystallization was simulated by cooling in a system initially at the QFM buffer but then closed to oxygen. The variation of normal series glass compositions is well-modeled by fractional crystallization at 500 b (Figures 8 and 9). Correlation between MgO and Al_2O_3 in the rock suite requires precipitation of plagioclase + olivine, and MELTS predicts plagioclase as the liquidus phase, closely followed by coprecipitation of olivine. The lack of correlation between CaO/Al_2O_3 and MgO precludes large amounts of clinopyroxene fractionation, and the MELTS model only predicts 5% clinopyroxene crystallization between 6.0%< MgO < 7.6% at low pressures. These results require that crystallization take place at low pressures (<1 kb) and low water contents (<0.4%), because higher pressures and water concentrations enhance clinopyroxene and suppress plagioclase crystallization in these

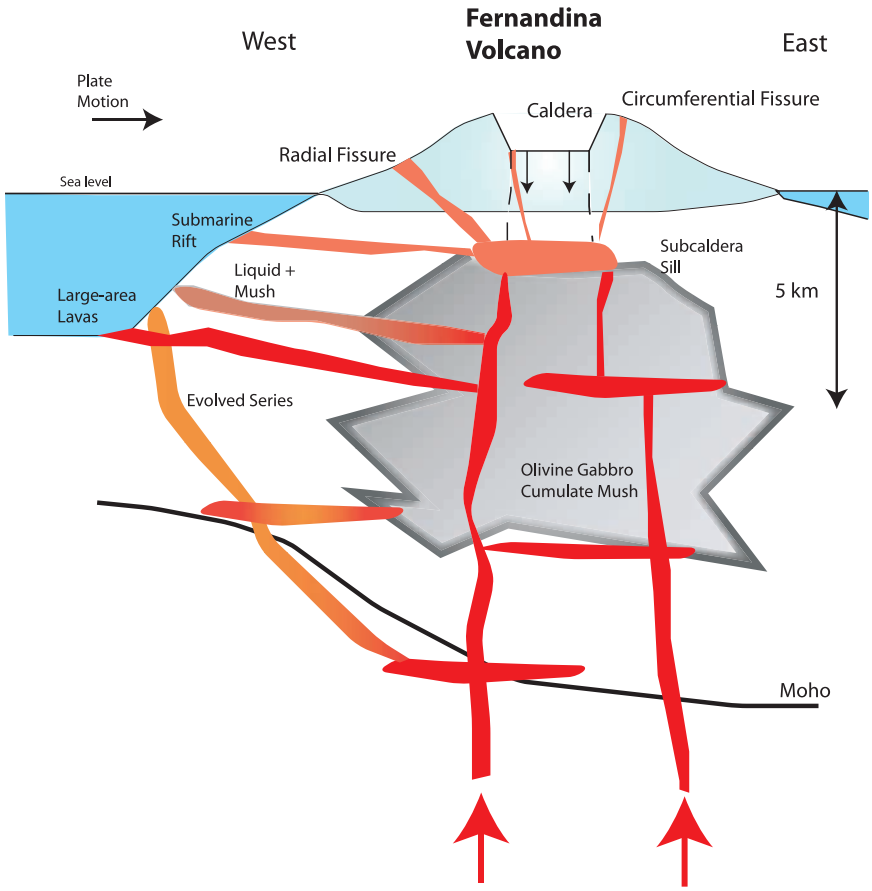

Figure 15. Conceptual model of Fernandina's magmatic plumbing system. A magma lens at ~1500 m below sea level feeds homogenized, olivine-poor lavas to circumferential fissures near the summit and diffuse radial fissures on the lower flanks. A thick pile of super-solidus olivine-gabbro mush is deposited by the uppermost sill and possibly other magma bodies in the midcrust. Reaction with the mush and homogenization by magma mixing in the magma bodies buffer compositions of the magmas from the time they enter the crust, resulting in a compositionally monotonous normal series of magmas that feed both subaerial and submarine eruptions on and around Fernandina. Magmas are also injected laterally into the submarine rifts and the deep seafloor west of the island; some of these magmas erode olivine-gabbro mush from the basal part of the storage chamber, resulting in the eruption of porphyritic lavas (including some picrites). Some magmas bypass the central magmatic system and evolve by cooling and crystallization in the upper mantle and lower crust, forming the evolved series. Position of the Moho is from *Feighner and Richards* [1994].

compositions [*Geist et al.*, 1998]. We suggest that all of the normal-series and subaerial magmas equilibrate in the 2-km deep subcaldera magma chamber, which has been delineated from deformation studies [*Amelung et al.*, 2000; *Geist et al.*, 2006].

[37] Differences between the glasses and whole-rock compositions in both the subaerial and submarine suites can be explained by addition of plagioclase, olivine, and augite in varying proportions to glass compositions (Figure 8). This hypothesis was tested statistically by performing a least squares analysis relating each of the whole-rock analyses to an average glass composition by adding mineral compositions. The predicted addition ranges from 0 to 20% for olivine, 6 to 22% for plagioclase, and <10% for augite, consistent with the lavas' petrography; the sum of the square of the residuals ranges from 0.02 to 0.48. These tests, along with the zoning profiles and equilibrium calculations, show that most of the "phenocrysts" in these lavas are in fact exotic. Most lavas consist of liquids bearing crystals that did not form directly from the host liquid.

[38] The accumulation of olivine in submarine lavas of the normal series is likely to result from

a "flushing" process, because lateral intrusion is more capable of carrying the dense olivine than is vertical ascent [cf. *Marsh*, 2005]. The width of narrowly zoned rims on olivine xenocrysts limits the time that the crystals could have been contained within their host liquids. For example, the most forsteritic olivine in sample AHA29A has a normally zoned rim that is < 20 microns thick (Figure 13). Glass of AHA29A composition is in equilibrium with Fo_{73}. The MgO-FeO diffusion coefficient calculated by the method of *Danyushevsky et al.* [2002], assuming that T = 1150° C and the olivine's composition is Fo_{86}, is $2.9 \times 10^{-17} m^2/s$. Under these boundary conditions, a compositional boundary layer (90% equilibrated) that is 20 microns thick at the olivine rim develops in about 6 months. The thickest zoned rims are observed in olivines with cores of Fo_{83}, which have rims that are ~ 30 microns thick, indicating residence times of about a year. Again, the crystals in sample AHA29A are typical of those in all of the normal-series rocks, none of which contains olivine that shows a systematic equilibrium relationship with its host glass or has a consistent zoning patterns. Thus we conclude that the "phenocrysts" within these submarine basalts are largely unrelated to the glasses that host them and were probably entrained within their host lavas less than a year before eruption.

6.4. Origin of the Evolved Series

[39] The evolved series lavas that erupted from the southwest sector of Fernandina do not lie on the same trends on chemical variation diagrams that describe the normal series (Figures 7 and 8). Instead, they have relatively high Al_2O_3 concentrations and low FeO and TiO_2 concentrations (Figure 8). Nevertheless, evolved series lavas have trace element patterns that are parallel to those of the normal series (Figures 10 and 11), suggesting that evolved and normal series magmas are cogenetic. A MELTS simulation of crystallization of sample D28C (7.6% MgO) at 5 kb replicates the trend formed by the evolved series, particularly the enrichment in Al_2O_3. The model predicts that after 58% crystallization of an assemblage that is 68% augite, 27% plagioclase, and 5% magnetite, a liquid with 3.2% MgO and 16.6% Al_2O_3 is produced. The model was tested by applying these values to a trace element model (Figure 11), and the observed patterns are reproduced.

[40] Unlike the majority of submarine normal-series lavas, these evolved magmas did not develop by extensive crystallization of plagioclase in the shallow subcaldera magma chamber. Instead, the evolved series magmas result from extensive fractional crystallization in the upper mantle and lower crust (the depth to the Moho beneath Fernandina is ~14 km; P ~3.5 kb [*Feighner and Richards*, 1994]), and bypassed the shallow magmatic plumbing system beneath the volcano (Figure 15).

6.5. Origins of the High-K Lava

[41] Rocks from D27 at the foot of Fernandina's southwest rift (Figure 3) have high K_2O and Al_2O_3 concentrations and low FeO and CaO (Figure 8). D27 is from the region where evolved series lavas were recovered (Figure 3), but D27 glasses have MgO 5.6% to 5.8%. A least squares minimization indicates that the composition of D27A can be produced by a 48:52 mixture of normal-series D28C (7.59% MgO) and evolved-series D17bur (4.48% MgO), with a sum of the square of residuals being 1.2%. Thus we propose that the high-K magma results from a body of normal series magma that mixed with a body of evolved series magma at the distal end of the southwest rift (Figure 15). Petrographically, D27 is not unusual, with abundant microphenocrysts of augite and plagioclase; no megacrysts with embayments, sieve textures, or unusual zoning patterns are apparent. Efficient crystal segregation must have occurred after the mafic and evolved magmas hybridized, removing petrographic evidence for magma mixing.

6.6. Implications for Fernandina's Subcaldera Plumbing System

[42] The geochemistry and petrology of normal series and subaerial lavas indicate a quasi-steady state magma body, whose top lies ~ 2 km beneath Fernandina's caldera floor (~1500 m below sea level, Figure 15) [*Amelung et al.*, 2000; *Geist et al.*, 1998, 2006]. The magma undergoes crystallization of plagioclase + olivine ± clinopyroxene, but is continually replenished by magma that precipitates olivine as magnesian as Fo_{89} (Mg# ~ 70).

[43] At Fernandina, the phenocryst assemblage is dominated by plagioclase in the subaerial environment but a mixture of olivine + plagioclase + augite in the submarine environment (Figure 6). The petrographic observations and petrologic modeling presented here suggest that most of Fernandina's lavas are hybrids between liquid magma and exotic crystals, especially when the submarine lavas are compared to the subaerial lavas studied

by *Allan and Simkin* [2000]. Another important observation is that the normal-series submarine lavas contain no xenoliths, but instead bear single crystals and glomerocrysts, indicating that the entrained crystals do not come from cumulate rocks, but more likely from a crystal mush [*Marsh*, 2005] that would more easily disaggregate.

[44] The systematic differences between subaerial and submarine lavas are best explained by gravitational sorting. A typical Fernandina liquid with 6.5% MgO has a calculated density of 2760 kg/m^3. The densities of plagioclase and olivine at magmatic temperatures are 2740 and 3370 kg/m^3. This results in plagioclase floating or being neutrally buoyant in the shallow subcaldera magma chamber, while olivine and pyroxene sink, are deposited at the chamber floor, and are incorporated into a growing column of mush. Magma intruded laterally incorporates mush rich in mafic minerals, whereas magma intruded upward only incorporates plagioclase (Figure 15).

7. Conclusions

[45] No seamount exists at the leading edge of the Galápagos hot spot (Figure 2), unlike other Pacific hot spots chains such as Samoa and Hawaii where seamounts represent the first manifestation of the hot spot as the lithosphere travels over the mantle source [e.g., *Moore et al.*, 1982; *Hart et al.*, 2000]. Instead, the deep seafloor west of Fernandina volcano is partially paved by voluminous lava flow fields derived from basaltic magmas that are related to those of the subaerial volcano. An important new finding is that linear rift zones are well developed on the submarine flanks of Fernandina, in addition to Ecuador and Wolf volcanoes. The prominent submarine rifts contrast with diffuse radial rifts on the lower subaerial slopes of Galápagos volcanoes and ring fractures proximal to the summit calderas. This systematic change in orientation of fissures at Fernandina and focusing of the rifts in the submarine environment reflect the change in orientation and increasing magnitude of the deviatoric stresses in the shallow crust generated by the growing subaerial shield volcano.

[46] Most magmas erupted from the submarine flanks of Fernandina are genetically related to differentiated tholeiites erupted from the subaerial edifice [*Allan and Simkin*, 2000] by entrainment of different assemblages of crystals. Compositions of subaerial liquids are identical to those that form the submarine "normal series". The common genesis and evolution of subaerial and submarine magmas is best explained if the submarine lavas are emplaced by lateral injection of magmas that originally ascend beneath the central subcaldera edifice (Figure 15), a process similar to the origin of lavas erupted from Kilauea's Puna Ridge [*Dixon and Clague*, 2001; *Johnson et al.*, 2002]. The sole difference between Fernandina's subaerial and submarine lavas is their crystal cargo, with the submarine lavas containing many more mafic crystals. This is best explained by a density-stratified magmatic plumbing system in which magmas derived from the lower parts of the storage system are injected laterally and encounter olivine-rich mush, whereas magmas ascending to the upper circumferential and subaerial radial fissures encounter plagioclase-rich mush.

[47] Differentiated magmas erupted from the submarine sector intruded from depth without encountering the shallow subcaldera plumbing system. Instead, they cooled and fractionated near the Moho to form differentiated tholeiite and icelandite liquids. At least one of these differentiated liquids hybridized with one of the more typical, shallowly differentiated liquids to create the high-K magma sampled from the tip of the SW rift.

[48] In conclusion, the petrogenesis of the submarine lavas at Fernandina is much more diverse than the subaerial ones. This diversity reveals processes that would not be understood, much less detectable, through study of only the emergent edifice. Likewise, measurements of the morphology of Fernandina's submarine sectors have led to the discovery of volcanic landforms that are not otherwise present on Galápagos shield volcanoes. Only through detailed petrologic and volcanologic study of both the subaerial edifice [*Rowland*, 1996; *Allan and Simkin*, 2000] and the submarine part of the volcano have we been able to deduce the fundamental processes responsible for the formation and evolution of this volcano at the leading edge of the Galápagos hot spot.

Acknowledgments

[49] We thank the officers and crews of R/V *Melville* and R/V *Revelle* of Scripps Institution of Oceanography (SIO) for excellent support in collecting the field data. Superb technical help at sea and for shore-based processing of sonar data by the Hawaii Mapping Research Group, which operates the MR1 side-scan sonar system, is gratefully acknowledged. Our work was aided by a great scientific team that included Josh Curtice, Jeremy Haney, Joe Liccardi, Rob Otto, Bob Reynolds, Paul Johnson, and Alberto Saal. SIO shipboard technical advice by

Ron Comer and Gene Pillard, who assisted with the dredging operations during the two cruises, was excellent; their dedication and knowledge helped ensure the success of our sampling operations. Uta Peckman of SIO provided exceptional support for merging multibeam data from various cruises to the area. Jenny Engels helped analyze data from the camera tow. We gratefully acknowledge the assistance of the students who participated on these cruises and helped with the watchstanding and sampling operations. Thanks to Scotty Cornelius for his adept work with the microprobe and Ellen Hedfield for her assistance. This work was supported by the National Science Foundation grants OCE0002818 and EAR0207605 (D.G.), OCE0002461 (D.J.F. and M.K.), OCE9811504 (D.J.F. and M.R.P.), and EAR0207425 (K.H.) and WHOI postdoctoral support for Soule. We appreciate and thank Vincent Salters and Mary Reid for their constructive editorial advice on this work.

References

Acosta, J., E. Uchupi, D. Smith, A. Munoz, P. Herranz, C. Palomo, P. Llanes, M. Ballesteros, and ZEE Working Group (2003), Comparison of volcanic rifts on La Palma and El Hierro, Canary Islands and the Island of Hawaii, *Mar. Geophys. Res.*, *24*, 59–90.

Allan, J. F., and T. Simkin (2000), Fernandina Volcano's evolved, well-mixed basalts: Mineralogical and petrological constraints on the nature of the Galápagos plume, *J. Geophys. Res.*, *105*, 6017–6031.

Allegre, C. J., T. Staudacher, P. Sarda, and M. Kurz (1983), Constraints on evolution of Earth's mantle from rare gas systematics, *Nature*, *303*, 762–766.

Amelung, F., S. Jonsson, H. Zebker, and P. Segall (2000), Widespread uplift and "trapdoor" faulting on Galápagos volcanoes observed with radar interferometry, *Nature*, *407*, 993–998.

Chadwick, W. W., and J. H. Dieterich (1995), Mechanical modeling of circumferential and radial dike intrusion on Galápagos volcanoes, *J. Volcanol. Geotherm. Res.*, *66*, 37–52.

Chadwick, W. W., and K. A. Howard (1991), The pattern of circumferential and radial eruptive fissures on the volcanoes of Fernandina and Isabela islands, Galápagos, *Bull. Volcanol.*, *53*, 259–275.

Christie, D. M., R. A. Duncan, A. R. McBirney, M. A. Richards, W. M. White, K. S. Harpp, and C. G. Fox (1992), Drowned islands downstream from the Galápagos hotspot imply extended speciation times, *Nature*, *355*, 246–248.

Clague, D. A., J. G. Moore, J. E. Dixon, and W. B. Friesen (1995), Petrology of submarine lavas from Kilauea's Puna Ridge, Hawaii, *J. Petrol.*, *36*, 299–349.

Clague, D. A., K. Uto, K. Satake, and A. S. Davis (2002), Eruption style and flow emplacement in the submarine North Arch Volcanic Field, Hawaii, in *Hawaiian Volcanoes: Deep Underwater Perspectives*, *Geophys. Monogr. Ser.*, vol. 128, edited by E. Takahashi et al., pp. 65–84, AGU, Washington, D. C.

Cullen, A. B., A. R. McBirney, and R. D. Rogers (1987), Structural controls on the morphology of Galápagos shields, *J. Volcanol. Geotherm. Res.*, *34*, 143–151.

Danyushevsky, L. V., S. Sokolov, and T. J. Falloon (2002), Melt inclusions in olivine phenocrysts: Using diffusive re-equilibration to determine the cooling history of a crystal, with implications for the origin of olivine-phyric volcanic rocks, *J. Petrol.*, *43*, 1651–1671.

Diefenbach, B. (2005), Volcanic construction of the Galápagos Platform: Evidence from morphology and geochemistry of large submarine terraces, M. S. thesis, Univ. of Idaho, Moscow.

Dieterich, J. H. (1988), Growth and persistence of Hawaiian rift zones, *J. Geophys. Res.*, *93*, 4258–4270.

Dixon, J. E., and D. A. Clague (2001), Volatiles in basaltic glasses from Loihi Seamount, Hawaii: Evidence for a relatively dry plume component, *J. Petrol.*, *42*, 627–654.

Feighner, M. A., and M. A. Richards (1994), Lithospheric structures and compensation mechanisms of the Galápagos Archipelago, *J. Geophys. Res.*, *99*, 6711–6729.

Fialko, Y. A., and A. Rubin (1999), What controls the along-strike slopes of volcanic rift zones?, *J. Geophys. Res.*, *104*, 20,007–20,020.

Fiske, R. S., and E. D. Jackson (1972), Orientation and growth of Hawaiian volcanic rifts: The effect of regional structure and gravitational stresses, *Proc. R. Soc. London, Ser. A*, *329*, 299–326.

Fornari, D. J., and J. F. Campbell (1987), Submarine topography around the Hawaiian Islands, in *Volcanism in Hawaii*, edited by R. W. Decker, T. L. Wright, and P. H. Stauffer, *U. S. Geol. Surv. Prof. Pap.*, *P-1350*, 109–124.

Fornari, D. J., D. W. Peterson, J. P. Lockwood, A. Malahoff, and B. C. Heezen (1979), Submarine extension of the southwest rift zone of Mauna Loa volcano, Hawaii: Visual observations from U. S. Navy deep submergence vehicle DSV Sea Cliff, *Geol. Soc. Am. Bull.*, *90*, 435–443.

Fornari, D. J., M. O. Garcia, R. C. Tyce, and D. G. Gallo (1988), Morphology and structure of Loihi seamount based on seabeam sonar mapping, *J. Geophys. Res.*, *93*, 15,227–15,238.

Fornari, D. J., M. D. Kurz, D. J. Geist, P. D. Johnson, U. G. Peckman, and D. Scheirer (2001), New perspectives on the structure and morphology of the submarine flanks of Galápagos volcanoes—Fernandina and Isabela, *Eos Trans. AGU*, *82*(47), Fall Meet. Suppl., Abstract T41D-06.

Garcia, M. O., T. P. Hulsebosch, and J. M. Rhodes (1995), Olivine-rich submarine basalts from the southwest rift zone of Mauna Loa volcano: Implications for magmatic processes and geochemical evolution, in *Mauna Loa Revealed: Structure, Composition, History, and Hazards*, *Geophys. Monogr. Ser.*, vol. 92, edited by J. M. Rhodes and J. P. Lockwood, pp. 219–239, AGU, Washington, D. C.

Garcia, M. O., K. H. Rubin, M. D. Norman, J. M. Rhodes, D. W. Graham, D. W. Muenow, and K. Spencer (1998), Petrology and geochronology of basalt breccia from the 1996 earthquake swarm of Loihi seamount, Hawaii: Magmatic history of its 1996 eruption, *Bull. Volcanol.*, *59*, 577–592.

Garcia, M. O., J. Caplan-Auerbach, E. H. De Carlo, K. D. Kurz, and N. Becker (2006), Geology, geochemistry and earthquake history of Loihi seamount, Hawaii's youngest volcano, *Chem. Erde*, *66*, 81–108.

Geist, D. J., T. R. Naumann, and P. L. Larson (1998), Evolution of Galápagos magmas: Mantle and crustal fractionation without assimilation, *J. Petrol.*, *39*, 953–971.

Geist, D., W. W. Chadwick, and D. J. Johnson (2006), Results from new GPS and gravity monitoring networks at Fernandina and Sierra Negra Volcanoes, Galápagos, 2000–2002, *J. Volcanol. Geotherm. Res.*, *150*, 79–97.

Ghiorso, M. S., and R. O. Sack (1995), Chemical mass transfer in magmatic processes IV: A revised and internally consistent thermodynamic model for the interpolation and extrapolation of liquid-solid equilibria in magmatic systems at elevated temperatures and pressures, *Contrib. Mineral. Petrol.*, *119*, 197–212.

Graham, D. W., D. M. Christie, K. S. Harpp, and J. E. Lupton (1993), Mantle plume helium in submarine basalts from the Galápagos platform, *Science*, *262*, 2023–2026.

Green, T. H. (1995), Significance of Nb/Ta as an indicator of geochemical processes in the crust-mantle system, *Chem. Geol.*, *120*, 347–359.

Gregg, T. K. P., and D. J. Fornari (1998), Long submarine lava flows: Observations and results from numerical modeling, *J. Geophys. Res.*, *103*, 27,517–27,531.

Gripp, A. E., and R. G. Gordon (2002), Young tracks of hotspots and current plate velocities, *Geophys. J. Int.*, *150*, 321–361.

Harpp, K. S., D. J. Fornari, D. J. Geist, and M. D. Kurz (2003), Genovesa Submarine Ridge: A manifestation of plume-ridge interaction in the northern Galápagos Islands, *Geochem. Geophys. Geosyst.*, *4*(9), 8511 doi:10.1029/2003GC000531.

Hart, S. R., et al. (2000), Vailulu'u undersea volcano: The New Samoa, *Geochem. Geophys. Geosyst.*, *1*(12), doi:10.1029/2000GC000108.

Hofmann, A. W. (1997), Mantle geochemistry: the message from oceanic volcanism, *Nature*, *385*, 219–229.

Holcomb, R. T., J. G. Moore, P. W. Lipman, and R. H. Belderson (1988), Voluminous submarine lava flows from Hawaiian volcanoes, *Geology*, *16*, 400–404.

Hooft, E. E., D. R. Toomey, and S. C. Solomon (2003), Anomalously thin transition zone beneath the Galápagos hotspot, *Earth Planet. Sci. Lett.*, *216*, 55–64.

Johnson, D. M., P. R. Hooper, and R. M. Conrey (1999), XRF analysis of rocks and minerals for major and trace elements on a single low dilution Li-tetraborate fused bead, *Adv. X-Ray Anal.*, *41*, 843–867.

Johnson, K. T. M., J. R. Reynolds, D. Vonderhaar, D. K. Smith, and L. S. L. Kong (2002), Petrological systematics of submarine basalt glasses from the Puna Ridge, Hawai'i: Implications for rift zone plumbing and magmatic processes, in Hawaiian Volcanoes: Deep Underwater Perspectives, *Geophys. Monogr. Ser.*, vol. 128, edited by E. Takahashi et al., pp. 143–159, AGU, Washington, D. C.

Jónsson, S., H. Zebker, P. Cervelli, P. Segall, H. Garbeil, P. Mouginis-Mark, and S. Rowland (1999), A shallow-dipping dike fed the 1995 flank eruption at Fernandina volcano, Galápagos, observed by satellite radar interferometry, *Geophys. Res. Lett.*, *26*(8), 1077–1080.

Kurz, M. D., and D. Geist (1999), Dynamics of the Galápagos hotspot from helium isotope geochemistry, *Geochim. Cosmochim. Acta*, *63*, 4139–4156.

Kurz, M. D., S. Rowland, J. Curtice, A. Saal, and T. Naumann (2005), Eruption rates at Fernandina volcano, Galápagos archipelago, from cosmogenic helium in surficial lava flows, *Eos Trans. AGU*, *86*(52), Fall Meet. Suppl., Abstract U33A-0016.

Lea, D. W., D. K. Pak, C. L. Belanger, H. J. Spero, and M. A. Hall (2006), Paleoclimate history of Galápagos surface waters over the last 135000 years, *Quat. Sci. Rev.*, *25*, 1152–1167.

Lenat, J., B. Gibert-Malengreau, and A. Galdeano (2001), A new model for the evolution of the volcanic island of Reunion (Indian Ocean), *J. Geophys. Res.*, *106*, 8645–8663.

Lipman, P. W., W. R. Normark, J. G. Moore, J. B. Wilson, and C. E. Gutmacher (1988), The giant submarine Alika debris slide, Mauna Loa, Hawaii, *J. Geophys. Res.*, *93*, 4279–4299.

Lipman, P. W., T. W. Sisson, T. Ui, J. Naka, and J. R. Smith (2002), Ancestral submarine growth of Kilauea Volcano and instability of its south flank, *Hawaiian Volcanoes: Deep Underwater Perspectives*, *Geophys. Monogr. Ser.*, vol. 128, edited by E. Takahashi et al., pp. 161–191, AGU, Washington, D. C.

Lonsdale, P. (1989), A geomorphological reconnaissance of the submarine part of the east rift zone of Kilauea volcano, Hawaii, *Bull. Volcanol.*, *51*, 123–144.

Malahoff, A. (1987), Geology of the summit of Loihi submarine volcano: Volcanism in Hawaii, *U. S. Geol. Surv. Prof. Pap.*, *1350*, 133–144.

Marsh, B. (2005), A magmatic mush column Rosetta Stone: The McMurdo dry valleys of Antarctica, *Eos Trans. AGU*, *85*, 497–502.

McBirney, A. R., and H. Williams (1969), Geology and petrology of the Galápagos Islands, *Mem. Geol. Soc. Am.*, *118*, 197 pp.

Moore, J. E., D. A. Clague, R. T. Holcomb, P. W. Lipman, W. R. Normark, and M. E. Torresan (1989), Prodigious submarine landslides on the Hawaiian Ridge, *J. Geophys. Res.*, *94*, 17,465–17,484.

Moore, J. G., D. A. Clague, and W. R. Normark (1982), Diverse basalt types from Loihi seamount, Hawaii, *Geology*, *10*, 88–92.

Mouginis-Mark, P. J., S. K. Rowland, and H. Garbeil (1996), Slopes of western Galápagos volcanoes from airborne interferometric radar, *Geophys. Res. Lett.*, *23*, 3767–3770.

Naumann, T., and D. Geist (2000), Physical volcanology and structural development of Cerro Azul volcano, Isabela island, Galápagos: Implications for the development of Galápagos-type shield volcanoes, *Bull. Volcanol.*, *61*, 497–514.

Normark, W. R., J. G. Moore, and M. E. Torresan (1993), Giant volcano-related landslides and the development of the Hawaiian islands: Submarine landslides, in *Selected Studies in the U. S. Exclusive Economic Zone*, *U. S. Geol. Surv. Bull.*, *2002*, 184–196.

Perfit, M. R., and W. W. Chadwick, Jr. (1998), Magmatism at mid-ocean ridges: Constraints from volcanological and geochemical investigations, in *Faulting and Magmatism at Mid-Ocean Ridges*, *Geophys. Monogr. Ser.*, vol. 106, edited by W. R. Buck et al., pp. 59–116, AGU, Washington, D. C.

Rongstadt, M. (1992), HAWAII MR-1: A new underwater mapping tool, paper presented at International Conference on Signal Processing and Technology, Inst. of Electr. and Electron. Eng., San Diego, Calif.

Rowland, S. K. (1996), Slopes, lava flow volumes, and vent distributions on Volcán Fernandina, Galápagos Islands, *J. Geophys. Res.*, *101*, 27,657–27,673.

Simkin, T. (1972), Origin of some flat topped volcanoes and guyots, *Mem. Geol. Soc. Am.*, *132*, 183–193.

Simkin, T., and K. A. Howard (1970), Caldera collapse in the Galápagos islands, *Science*, *169*, 429–437.

Simkin, T., and L. Siebert (1994), *Volcanoes of the World*, 2nd ed., 349 pp., Geoscience, Tucson, Ariz.

Sisson, T. W., P. W. Lipman, and J. Naka (2002), Submarine alkalic through tholeiitic shield-state development of Kilauea Volcano, Hawai'i, *Hawaiian Volcanoes: Deep Underwater Perspectives*, *Geophys. Monogr. Ser.*, vol. 128, edited by E. Takahashi et al., pp. 193–219, AGU, Washington, D. C.

Smith, D. K., L. S. L. Kong, K. T. M. Johnson, and J. R. Reynolds (2002), Volcanic morphology of the submarine Puna Ridge, Kilauea Volcano. *Hawaiian Volcanoes: Deep Underwater Perspectives*, *Geophys. Monogr. Ser.*, vol. 128, edited by E. Takahashi et al., pp. 125–142, AGU, Washington, D. C.

Soule, S. A., D. J. Fornari, M. R. Perfit, M. A. Tivey, W. I. Ridley, and H. Schouten (2005), Channelized lava flows at the East Pacific Rise crest 9°–10°N: The importance of off-axis lava transport in developing the architecture of young

oceanic crust, *Geochem. Geophys. Geosyst.*, *6*, Q08005, doi:10.1029/2005GC000912.

Sun, S.-S., and W. F. McDonough (1989), Chemical and isotopic systematics of oceanic basalts: Implications for mantle compositions and processes, *Geol. Soc. Spec. Publ.*, *42*, 313–345.

Toomey, D. R., E. E. Hooft, S. C. Solomon, D. E. James, and M. L. Hall (2001), Upper mantle structure beneath the Galápagos archipelago from body wave data, *Eos Trans. AGU*, *82*(47), Fall Meet. Suppl., Abstract T41D-04.

White, W. M. (1985), Sources of oceanic basalts: Radiogenic isotope evidence, *Geology*, *13*, 115–118.